Assessment of Thermal Boundary Models for Large Eddy Simulations of Natural Convection

Lise Ceresiat[1*] and Miltiadis V. Papalexandris[1]

[1]Institute of Mechanics, Materials and Civil Engineering, Université catholique de Louvain, 1348, Louvain-la-Neuve, Belgium.

*Corresponding author(s). E-mail(s): lise.ceresiat@uclouvain.be;
Contributing authors: miltos@uclouvain.be;

Abstract

In this paper, we report on the efficacy of four different thermal boundary models for Wall-Modelled Large Eddy Simulations (WMLES) of turbulent natural convection. Our test cases consist of Rayleigh-Bénard convection of liquid water at two Rayleigh numbers, $\boldsymbol{Ra = 1.35\times10^8}$ and $\boldsymbol{Ra = 10^9}$, respectively. Two configurations are examined, namely, convection in a box and in a cavity; the latter one involving a free-slip top boundary. For these test cases, the numerical results obtained via WMLES with the thermal boundary models are compared with those of Wall-Resolved Large-Eddy Simulations (WRLES). According to our comparative studies, a particular version of the so-called Kays & Crawford model provides the most accurate predictions, at least for the test cases considered herein. Additionally, in this paper, we report on WMLES of turbulent convection at a higher Rayleigh number, $\boldsymbol{Ra = 5\times10^9}$, with the aforementioned model. For this case, we analyse herein the flow structure and present results for first and second-order statistics of the flow.

Keywords: Turbulent convection; wall models; large eddy simulations; boundary layers; convection in a cavity.

1 Introduction

Natural convection is a fundamental process of heat transfer that is encountered in numerous natural phenomena and industrial applications. For example, it plays a paramount role in atmospheric and oceanic flows (Marshall and Schott, 1999; Hartmann et al., 2001), airflow in the interior of buildings (Ramponi and Blocken, 2012), cooling of electronic devices and diverse engineering applications (Baïri et al., 2014; Sarbu and Dorca, 2019). Additionally, natural convection plays a significant role in thermal power stations and nuclear plants (*e.g.* in nuclear reactors and storage pools of spent fuel).

In most practical applications, natural convection occurs at high turbulence intensities, *i.e.* at high Rayleigh numbers. Therefore, an understanding of the properties of natural convection under such conditions is important. The classical study case is the so-called Rayleigh-Bénard Convection (RBC), which is convection between two horizontal boundaries kept at fixed temperatures (hot bottom boundary and cold top one); see for instance Ahlers et al. (2009); Chillà and Schumacher (2012); Grossmann and Lohse (2001, 2000, 2011); Lohse and Xia (2010); Niemela et al. (2000);

Bodenschatz et al. (2000); Wang et al. (2021). The Rayleigh number is a measure of the turbulence intensity and its definition is provided in section 2 below. Roughly speaking, RBC is turbulent for $Ra > 5{\times}10^5$. However, in most practical applications the Rayleigh number is far greater, namely, $Ra > 10^9$.

Numerical simulations are a promising method to investigate RBC. In Direct Numerical Simulations (DNS), the computational mesh is sufficiently fine to resolve turbulent scales of the flow. Thus far, DNS has provided significant insight into natural convection at low and moderate turbulence intensities. For example, Valencia et al. (2005, 2007) examined the transition from laminar to turbulent flow. Lohse and Xia (2010) and Shishkina and Thess (2009) studied the properties of the various turbulent structures, while Shishkina (2021) and Ahlers et al. (2022) investigated the effect of shape and aspect ratio of the flow domain. Also, DNS of natural convection in cavities have been performed by Hay and Papalexandris (2019) and Marichal and Papalexandris (2022). However, since the Rayleigh number scales with the cubic power of the domain height, the computational cost of DNS for most cases of practical interest is prohibitively high.

The Large Eddy Simulation (LES) approach offers a promising lower-cost alternative for reliable numerical studies of natural convection at high Rayleigh numbers. According to this approach, the governing equations are filtered and solved at coarser computational grids. In this manner, the large turbulent scales are directly resolved by the grid, while the effects of the small unresolved scales are suitably modelled via additional terms in the filtered equations. Early LES studies of RBC in a box were carried out by Eidson (1985) who employed a subgrid model for the thermal fluctuations based on the concept of the turbulent Prandtl number Pr_t (whose definition is given in section 3 below). Afterwards, several other studies focused on the development of thermal subgrid model for buoyancy-driven flow, *e.g.* Wong and Lilly (1994); Peng and Davidson (2002); Lau et al. (2012).

While LES offers significant computational savings in terms of resolving the turbulent flow structures (Peng and Davidson, 2001; Peng et al., 2006; Kenjereš and Hanjalić, 2006), it must still account for the boundary layers of the flow. The most accurate treatment is to employ sufficiently fine meshes to fully resolve the boundary-layer regions (Shishkina et al., 2010; Choi and Moin, 2012). This approach is called Wall-Resolved Large Eddy Simulations (WRLES) and can be computationally expensive. An alternative approach is to employ suitable models for the profiles of the flow variables in the boundary layers which is called Wall-Modelled Large Eddy Simulations (WMLES). Wall models (also referred to as wall functions) were initially developed for the hydrodynamic boundary layers; see, for example, the papers of Cabot and Moin (2000); Piomelli and Balaras (2002); Kawai and Larsson (2012); Larsson et al. (2016); Bose and Park (2018), as well as the monograph of Sagaut (2006).

Wall models have also been proposed for the thermal boundary layers (Kader, 1981; Silva et al., 1999; Sarić et al., 2017). However, they have been applied mostly in forced convection. So far, their efficacy for natural convection has been investigated to a much lesser extent. This is especially so in the case of free-slip boundaries. This type of boundary is typically employed to approximate the upper free surface in natural convection of liquids in cavities and pools (Zikanov et al., 2002; Hay and Papalexandris, 2019). The most significant feature of such a boundary is the development of a thermal boundary layer in the absence of a hydrodynamic one.

The main objective of this study is to assess four well-known thermal models for WMLES of natural convection. To this end, we consider cases of turbulent convection both in a box and in a cubic cavity. In the former case, the top boundary is a rigid wall, while in the latter one, it is a

free-slip plane. Therefore, concerning terminology, we do not refer to the thermal models as "wall models" but as "boundary models". Herein, we compare the predictions of WMLES with those of WRLES for the convection of water in a box and in a cavity at two different Rayleigh numbers, namely, $Ra = 1.35{\times}10^8$ and 10^9. Additionally, we present WMLES results for convection of water at a higher Rayleigh number, $Ra = 5{\times}10^9$ by employing the thermal boundary model which performed the best. The purpose of this simulation is to explore further the robustness of WMLES and to gain additional physical insight. It is worth noting that, to our knowledge, numerical results for RBC of fluids with $Pr > 1$ at such high Rayleigh numbers are currently unavailable.

This paper is structured as follows. In section 2, we present the governing equations. In section 3, we provide the outline of the subgrid models and the wall model for the hydrodynamic boundary layer that we have employed in our simulations. In the same section, we describe the four thermal boundary models under consideration. In section 4, we provide information for the computational grids and the numerical setup. Section 5 contains the numerical results; more precisely, the comparative studies of RBC in a box and in a cavity and the WMLES at $Ra = 5{\times}10^9$. Finally, section 6 concludes.

2 Governing equations

In our study the governing system of equations is the low-Mach number approximation of the compressible Navier-Stokes equations; see, for instance, Paolucci (1982) and Lessani and Papalexandris (2006). Since our study concerns LES of variable density flows, we employ the density-weighted or Favre filtering operator. For a generic quantity ϕ, the corresponding Favre-filtered quantity $\tilde{\phi}$ is given by $\tilde{\phi} = \frac{\overline{\rho\phi}}{\overline{\rho}}$, where the overbar sign denotes a spatially filtered quantity. In dimensional form, the filtered low-Mach number equations read

$$\frac{\partial \overline{\rho}}{\partial t} + \nabla \cdot (\overline{\rho}\widetilde{\boldsymbol{u}}) = 0\,, \tag{1}$$

$$\frac{\partial (\overline{\rho}\widetilde{\boldsymbol{u}})}{\partial t} + \nabla \cdot (\overline{\rho}\widetilde{\boldsymbol{u}}\widetilde{\boldsymbol{u}}) + \nabla \overline{p} = \nabla \cdot \widetilde{\boldsymbol{\tau}} - \nabla \cdot \boldsymbol{\tau}^r + \overline{\rho}\boldsymbol{g}\,, \tag{2}$$

$$c_p \frac{\partial (\overline{\rho}\widetilde{T})}{\partial t} + c_p \nabla \cdot (\overline{\rho}\widetilde{\boldsymbol{u}}\widetilde{T}) = \frac{dp_0(t)}{dt} + \nabla \cdot \widetilde{\boldsymbol{q}} - \nabla \cdot \boldsymbol{q}^r\,. \tag{3}$$

Following standard notation, ρ denotes the fluid density, $\boldsymbol{u} = (u, v, w)$ the velocity vector, p_0 the thermodynamics pressure, $\overline{p}$ the sum of the dynamic and bulk-viscous pressures (Papalexandris, 2020), c_p the specific heat capacity, and $\boldsymbol{g}$ the vector of gravitational acceleration which points to the negative y direction. Further, $\widetilde{\boldsymbol{\tau}}$ and $\widetilde{\boldsymbol{q}}$ are, respectively, the filtered viscous-stress tensor and heat-flux vector. These are given by

$$\widetilde{\boldsymbol{q}} = \lambda \nabla \widetilde{T}, \tag{4}$$

$$\widetilde{\boldsymbol{\tau}} = 2\mu \left(\widetilde{\boldsymbol{S}} - \frac{1}{3}(\nabla \cdot \widetilde{\boldsymbol{u}})\boldsymbol{I} \right)\,, \tag{5}$$

where μ is the dynamic viscosity, λ the heat conductivity, $\boldsymbol{I}$ the identity matrix and $\widetilde{\boldsymbol{S}}$ the filtered strain-rate tensor, $\widetilde{\boldsymbol{S}} = \frac{1}{2}\left(\nabla \widetilde{\boldsymbol{u}} + (\nabla \widetilde{\boldsymbol{u}})^\top\right)$. Whereas $\boldsymbol{\tau}^r$ and $\boldsymbol{q}^r$ are, respectively, the subgrid stress tensor and heat flux. They are defined by

$$\boldsymbol{\tau}^r = \overline{\rho}\,(\widetilde{\boldsymbol{u}\boldsymbol{u}} - \widetilde{\boldsymbol{u}}\widetilde{\boldsymbol{u}})\,, \tag{6}$$

$$\boldsymbol{q}^r = \overline{\rho} c_p (\widetilde{\boldsymbol{u}T} - \widetilde{\boldsymbol{u}}\widetilde{T})\,, \tag{7}$$

and need to be modelled.

In the present study, the working fluid is liquid water. Since its compressibility is very low, the thermodynamic pressure p_0 is considered constant, and its density ρ is assumed to be a function of the temperature only. To account for the variations of density, heat capacity c_p and transport properties (μ and λ) with temperature, we employ a fourth-order polynomial fit of tabulated data for the quantity at the presumed thermodynamic pressure and over the temperature range of interest from the database of Lemmon et al. (2010),

$$\overline{\phi} \;=\; c_4\widetilde{T}^4 + c_3\widetilde{T}^3 + c_2\widetilde{T}^2 + c_1\widetilde{T} + c_0\,. \tag{8}$$

The coefficients of the polynomial fit are summarized in Table 1 below.

Table 1 Polynomial coefficients for variable liquid water properties from the database of Lemmon et al. (2010) over the temperature range 347.95 to 370.65 K.

	c_4	c_3	c_2	c_1	c_0
ρ	-3.36×10^{-8}	5.3×10^{-5}	-3.35×10^{-2}	9.13	113.2
c_p	1.67×10^{-7}	-2.36×10^{-4}	0.14	-35.76	7768.09
μ	3.19×10^{-12}	-4.95×10^{-9}	2.91×10^{-6}	-7.67×10^{-4}	7.72×10^{-2}
λ	-3.29×10^{-11}	5.71×10^{-8}	-4.26×10^{-5}	1.52×10^{-2}	-1.39

We consider natural convection in a box and in a cubic cavity. In both configurations, the bottom wall is maintained at a given temperature while the top boundary (being a rigid wall in the case of a box and a free-slip plane in the case of a cavity) is maintained at a lower temperature, thereby inducing convective motions of the working fluid. The relevant dimensionless groups in RBC in cubic domains are the Rayleigh and Prandtl numbers which are defined as

$$Ra \;=\; \frac{|\boldsymbol{g}|\rho\beta\Delta T L^3}{\mu\alpha}\,, \qquad\qquad Pr \;=\; \frac{\mu c_p}{\lambda}\,, \tag{9}$$

respectively. In the definition of the Rayleigh number, ΔT is the temperature difference between the top and bottom boundaries and L is the distance between them (*i.e.* the domain height).

The governing systems of equations (1)-(3) is solved numerically via the time-accurate algorithm of Lessani and Papalexandris (2006). It is based on a second-order predictor-corrector scheme for integration in time and employs a projection (fractional-step) method for the computation of the pressure and velocity fields. More specifically, the divergence of the momentum equation (2), results in a constant-coefficient Poisson equation for the pressure. Upon discretization, the Poisson equation is reduced to a sparse linear system that is solved via an iterative linear-system solver. Spatial derivatives are discretized via second-order centred differences. The algorithm is implemented in a collocated-grid arrangement and utilizes a flux-interpolation technique (Lessani and Papalexandris, 2006, 2008) to avoid the problem of pressure odd-even decoupling that is often encountered with such grids. The algorithm has been implemented in a C/C++ code which is parallelized via the MPI protocol and uses the PETSc library of data structures and linear-solvers (Balay and Abhyankar, 2019). The Poisson equation for the pressure is solved with the PETSc routine of PFMG which is a parallel semicoarsening multigrid solver.

3 Subgrid and wall models

Typically, the subgrid stress tensor $\boldsymbol{\tau}^r$ and heat flux $\boldsymbol{q}^r$ are modelled via the eddy-viscosity approach (Sagaut, 2006). According to it, $\boldsymbol{\tau}^r$ represents additional viscous stresses and therefore its deviatoric component is modelled as

$$\boldsymbol{\tau}^r - \frac{1}{3}\mathrm{tr}(\boldsymbol{\tau}^r)\boldsymbol{I} \;=\; 2\mu_{\mathrm{sgs}}\left(\widetilde{\boldsymbol{S}} - \frac{1}{3}(\nabla\cdot\widetilde{\boldsymbol{u}})\boldsymbol{I}\right). \tag{10}$$

Whereas the isotropic component $\frac{1}{3}\mathrm{tr}(\boldsymbol{\tau}^{\mathrm{r}})\boldsymbol{I}$, often referred to as the residual kinetic energy, is incorporated in the pressure term $\overline{p}$ of equation (2). In our study, the turbulent eddy viscosity μ_{sgs} is computed via the Wall-Adapting Local Eddy-viscosity (WALE) model of Nicoud and Ducros (1999),

$$\mu_{\mathrm{sgs}} \;=\; \overline{\rho}(C_w\Delta)^2\frac{\left(\widetilde{\boldsymbol{\mathcal{S}}}^d:\widetilde{\boldsymbol{\mathcal{S}}}^d\right)^{3/2}}{\left(\widetilde{\boldsymbol{S}}:\widetilde{\boldsymbol{S}}\right)^{5/2}+\left(\widetilde{\boldsymbol{\mathcal{S}}}^d:\widetilde{\boldsymbol{\mathcal{S}}}^d\right)^{5/4}}. \tag{11}$$

In the above equation, $\widetilde{\boldsymbol{\mathcal{S}}}^d$ is the traceless symmetric part of the square of the velocity-gradient tensor $\widetilde{\boldsymbol{\mathcal{S}}}$. In other words,

$$\widetilde{\boldsymbol{\mathcal{S}}}^d \;=\; \frac{1}{2}\left(\widetilde{\boldsymbol{\mathcal{S}}}+\widetilde{\boldsymbol{\mathcal{S}}}^{\top}\right)-\frac{1}{3}\mathrm{tr}(\widetilde{\boldsymbol{\mathcal{S}}})\boldsymbol{I}, \quad \text{with} \quad \widetilde{\boldsymbol{\mathcal{S}}} \;=\; (\nabla\boldsymbol{u})\cdot(\nabla\boldsymbol{u}). \tag{12}$$

Also, in equation (11) above, Δ is the filter width, defined as the cubic root of the volume of a given computational cell, $\Delta = (\Delta x\,\Delta y\,\Delta z)^{1/3}$. Further, C_w is the model constant and is set at $C_w = 0.325$ (Nicoud and Ducros, 1999). Finally, the double-dot symbol stands for the double inner product between two second-order tensors.

Within the framework of our study, we also performed wall-resolved LES of natural convection using the classical Smagorinsky model with constant coefficient (Ferziger et al., 2019) and the dynamic Lagrangian model of Meneveau et al. (1996). The results obtained with the classical Smagorinsky model were less accurate than with the other two models. Whereas, the WALE and dynamic Lagrangian models yielded results of comparable accuracy. In our simulations, we opted to employ the WALE model due to its simplicity.

With regard to the subgrid heat flux $\boldsymbol{q}^r$ in equation (7), according to the eddy viscosity approach, it is modelled as

$$\boldsymbol{q}^r \;=\; \lambda_{\mathrm{sgs}}\nabla\widetilde{T}, \tag{13}$$

where λ_{sgs} is the turbulent heat conductivity coefficient. This coefficient is calculated via the Reynolds analogy, according to which

$$Pr_t \;=\; \frac{\mu_{\mathrm{sgs}}c_p}{\lambda_{\mathrm{sgs}}}, \tag{14}$$

where Pr_t is the turbulent Prandtl number. In our study, Pr_t is assumed to be constant and equal to 0.4 as recommended by Eidson (1985).

While WRLES allows a coarser grid in the bulk region, the grid resolution near solid boundaries still needs to be fine enough so as to sufficiently resolve the boundary layers. With WMLES, the boundary layers are not resolved anymore. Instead, the effects of shear stresses and heat transfer are

approximated via wall models (also referred to as wall functions). These models rely on approximations of the structure of the viscous-wall region of hydrodynamic boundary layers, which is the region in which the viscous contributions to the shear stresses are significant (Pope, 2003). As mentioned in the Introduction, several wall models have been proposed in the past. Most of them were developed based on channel flows. Therefore, when applied in natural convection, one has to carefully assess how a particular wall model accounts for viscous dissipation inside the viscous wall region (Cabot and Moin, 2000; Piomelli and Balaras, 2002; Larsson et al., 2016; Sarić et al., 2017).

In our study, we employed the wall model of Cabot and Moin (2000). Similarly to subgrid modelling, wall models for the momentum equation typically incorporate a turbulent viscosity coefficient relative to the wall. This coefficient is a function of the distance from the wall, expressed in wall units y^+. The relation proposed by Cabot and Moin (2000) reads

$$\mu_t \;=\; \kappa\mu y^+ \left(1-\exp\left(-\frac{y^+}{A^+}\right)\right)^2 , \tag{15}$$

where κ and A^+ are, respectively, the von Karman and model constants. Their values are $\kappa = 0.41$ and $A^+ = 17$. The distance from the wall in wall units is given by $y^+ = (\rho u_\tau y)/\mu$, with u_τ being the friction velocity. The latter one is defined by $u_\tau = \sqrt{\tau_\mathrm{w}/\rho}$ where τ_w is the wall shear stress. In our study, the friction velocity is computed with the Reichardt (1961) relation which reads

$$u^+ \;=\; \frac{|u|}{u_\tau} \;=\; \frac{1}{\kappa}\ln\left(1+\kappa y^+\right) + B_1^+\left[1-\exp\left(-\frac{y^+}{B_2^+}\right)-\frac{y^+}{B_2^+}\exp\left(-\frac{y^+}{B_3^+}\right)\right] , \tag{16}$$

where the three model constants B_1^+, B_2^+ and B_3^+ are assigned the following values: $B_1^+ = 7.8$, $B_2^+ = 11$ and $B_3^+ = 3$. The values of the fluid velocity, density, and dynamic viscosity are taken at a point located sufficiently far from the wall but inside the boundary layer (Larsson et al., 2016). The distance of this point from the wall is referred to as the *exchange location* and is denoted herein by $y = h_\mathrm{wm}$. Since u_τ is given in terms of y^+, equation (16) constitutes a transcendental equation for u_τ which can be solved via an iteration scheme such as the Newton-Raphson method. Once solved, then the exchange location in wall units is computed via the following relation: $y^+_\mathrm{wm} = (\rho u_\tau h_\mathrm{wm})/\mu$. Next, the result is inserted in equation (15) to compute μ_t, the value of which replaces μ_sgs in the first layer of computational cells (next to the wall).

While numerous works have been devoted to the development of wall functions for the momentum equation, only a small number of studies focused on equivalent models for the energy equation (Benarafa et al., 2007). Furthermore, to our knowledge, the case of free-slip boundaries (at which there is a thermal layer but not a hydrodynamic one) has not been examined in the literature yet.

We now present the four thermal boundary models whose efficacy we assess herein. The first such model is based on the Reynolds Analogy (Eidson, 1985) and is referred to as RA. The model has already been employed for the modelling of the subgrid heat-flux vector in equation (14) above. The RA thermal model amounts to a modification of the value of the turbulent Prandtl number. According to it, the turbulent heat conductivity next to the wall is given by

$$\text{RA:} \qquad \lambda_t \;=\; \frac{\mu_t c_p}{Pr_t} \tag{17}$$

with the value for the turbulent Prandtl number set at $Pr_t = 0.9$ (Larsson et al., 2016). It is noted, however, that assuming a constant value of the turbulent Prandtl number inside the thermal

boundary layer can lead to inaccuracies because the fluid properties may vary locally due to strong temperature gradients.

Kays and Crawford (1993) proposed two thermal models based on experimental data. In the literature, they are referred to as "Kays & Crawford" models (Kays, 1994; Weigand et al., 1997). In this article, they are denoted by KC1 and KC2 respectively. The first model, KC1, was derived on the basis of flow measurements in the log-law region of the boundary layer at different Prandtl numbers. The second model, KC2, is derived from measurements of the flow properties in the viscous sub-layer of the boundary layer. These two models are given by

$$\text{KC1:} \qquad Pr_t = \frac{2}{Pr}\frac{\mu}{\mu_t} + 0.85\,, \tag{18}$$

$$\text{KC2:} \qquad Pr_t = \left(0.5882 + 0.228\left(\frac{\mu_t}{\mu}\right) - 0.0441\left(\frac{\mu_t}{\mu}\right)^2\left(1 - \exp\left(5.165\frac{\mu}{\mu_t}\right)\right)\right)^{-1}. \tag{19}$$

The fourth model examined in this study was proposed by Kader (1981) and is referred to as the Kader model. It is based on the concept of the friction temperature T_τ, which is analogous to the friction velocity. More specifically, T_τ is related to the surface heat flux q_w via the following relation: $q_\mathrm{w} = \rho c_p u_\tau T_\tau$. The Kader model also introduces an analogy between the temperature profile and the law of the wall for the velocity profile. According to it, starting from the wall, the temperature profile consists of a linear and a logarithmic contribution. More specifically, the difference between the temperature at a given point and the wall temperature, T_w, is given by

$$\frac{T_\mathrm{w} - T}{T_\tau} = Pr\; y^+ \exp(-\Gamma^+) + \left\{2.12\ln\left((1+y^+)C^+\right) + B^+\right\}\exp\left(-\frac{1}{\Gamma^+}\right). \tag{20}$$

In this equation, Γ^+, B^+ and C^+ are parameters that depend on the Prandtl number Pr, the distance in wall units y^+ and the thickness of the thermal boundary layer δ_θ:

$$\Gamma^+ = \frac{0.01(Pr\; y^+)^4}{1 + 5Pr^3\; y^+}\,, \tag{21}$$

$$B^+ = \left(3.85Pr^{1/3} - 1.3\right)^2 + 2.12\ln Pr\,, \tag{22}$$

$$C^+ = \frac{2.5\,(2 - y/\delta_\theta)}{1 + 4\,(1 - y/\delta_\theta)^2}\,. \tag{23}$$

Equation (20) is solved for the friction temperature T_τ in which y^+ and y are computed at the exchange location, *i.e.* at $y^+ = y^+_\mathrm{wm}$ and $y = y_\mathrm{wm}$. Subsequently, the turbulent heat conductivity λ_t at the first layer of computational cells, *i.e.* next to the wall, is computed via:

$$\text{Kader:} \qquad q_\mathrm{w} = \rho c_p u_\tau T_\tau = (\lambda_t + \lambda)\frac{dT}{dy}\,. \tag{24}$$

It is important to note that the Kader model assumes the presence of both a thermal and a hydrodynamic boundary layer. This is the case for zero-slip boundaries (walls). On the other hand, it cannot be applied in free-slip boundaries because they are characterized by the absence of a hydrodynamic layer. It is easily verified that the Kader model becomes singular when the friction velocity is zero.

4 Grid resolution and numerical setup

In this section, we elaborate on the grid resolution for our WMLES but also for the WRLES that is used as a benchmark in assessing the efficacy of the above-mentioned thermal models. In the following, the hat symbol $\hat{}$ is used to denote a dimensionless quantity. For non-dimensionalization purposes, the reference length is the height of the domain L. The reference velocity is the free-fall velocity, $u_{\rm ff} = \sqrt{|\boldsymbol{g}| L \beta_{\rm ref} \Delta T}$, with ΔT being the difference between the temperature of the heated bottom wall $T_{\rm h}$ and that of the top boundary $T_{\rm c}$, *i.*e. $\Delta T = T_{\rm h} - T_{\rm c}$. The reference time is the free-fall time, $t_{\rm ff} = L/u_{\rm ff}$. Also, the reference temperature is $T_{\rm ref} = (T_{\rm h} + T_{\rm c})/2$.

For both WMLES and WRLES the grid spacing in the bulk is determined based on the Taylor microscale of turbulent motions and the Batchelor scale which represents the size of the smallest thermal fluctuations. The Taylor microscale is estimated according to Peng et al. (2006),

$$\hat{\eta}_l \;=\; \frac{\sqrt{15}\,\hat{u}^*}{\sqrt{Ra\,(Nu-1)}}\,, \tag{25}$$

where $\hat{u}^*$ is representative of the dimensionless velocity in the bulk:

$$\hat{u}^* \;=\; \sqrt{0.068\,Ra^{0.91} + 0.012\,Ra^{0.96}}\,. \tag{26}$$

The Batchelor scale for a fluid with Prandtl number $Pr > 1$ is estimated by (Stevens et al., 2010),

$$\hat{\eta}_\theta \;=\; \left(\frac{1}{Ra\,Pr\,Nu}\right)^{1/4}\,. \tag{27}$$

The maximum length of a computational cell in the bulk is chosen to be the minimum between the half of the Taylor microscale, $\hat{\eta}_l/2$, and the relaxed temperature microscale, $4\pi\hat{\eta}_\theta$, (Hay et al., 2021).

Equations (25) and (27) require estimates for the (global) Nusselt number Nu. To this end, we have employed the following correlations $Nu - Ra$ for RBC in a box (Niemela et al., 2000) and in a cavity (Hay and Papalexandris, 2020),

$$\text{Box:} \qquad Nu \;=\; 0.124\,Ra^{0.309}\,, \tag{28}$$

$$\text{Cavity:} \qquad Nu \;=\; 0.178\,Ra^{0.301}\,. \tag{29}$$

Additionally, in WRLES the hydrodynamic and thermal boundary layers have to be fully resolved. The minimum number of grid cells inside the boundary layer is determined from the criterion of Shishkina et al. (2010) which is based on the Prandtl-Blasius theory for boundary layers. According to it, for $1 < Pr \leq 3$, the estimated dimensionless thicknesses of the hydrodynamic and thermal boundary layers read, respectively,

$$\hat{\delta}_u^{\rm es} \;=\; \frac{1}{2Nu}\,Pr^{(0.357 - 0.022\log Pr)}\,, \tag{30}$$

$$\hat{\delta}_\theta^{\rm es} \;=\; \frac{1}{2Nu}\,. \tag{31}$$

Then, the minimum numbers of grid cells required to resolve the boundary layers are

$$N_u \;=\; a\sqrt{2}Nu^{1/2}\,Pr^{(0.3215 + 0.011\ln Pr)}\,, \tag{32}$$

$$N_\theta \;=\; a\sqrt{2}Nu^{1/2}\,Pr^{(-0.0355 + 0.033\ln Pr)}\,, \tag{33}$$

with the model constant coefficient a set to $a = 0.482$. Subsequently, the computational grid is stretched (coarsened) from a wall towards the centre of the domain via a hyperbolic tangent function, in a manner that both the bulk and near-boundary resolution criteria are satisfied.

In WMLES, the grid resolution near wall boundaries depends on the thickness of the hydrodynamic boundary layer $\hat{\delta}_u$, estimated via equation (30), and the non-dimensional exchange location $\hat{h}_{\mathrm{wm}}$. As mentioned above, $\hat{h}_{\mathrm{wm}}$ has to lie inside the boundary layer. As a general guideline, it is set equal to 20% of the layer thickness; *i.*e. $\hat{h}_{\mathrm{wm}} = 0.2\hat{\delta}_u^{\mathrm{es}}$, see for example Kawai and Larsson (2012) and Larsson et al. (2016). This guideline has also been followed in the present study. Further, we set the exchange location point at the centre of the second layer of cells from the wall.

Since the computational domains in our study are cubic, we have used the same number of grid cells in all spatial directions, N. The properties of the grids used in our WMLES and WRLES are provided in Table 2. It should be mentioned that for RBC in a box at $Ra = 10^9$ with the same grid resolution as with the other models, the Kader model was prone to numerical instabilities. For this reason, and in this particular case, we had to increase the grid resolution in the WMLES involving the Kader model.

It is worth noting that with a decrease of 20% in the number of cells in each direction, the total number of grid cells is decreased to approximately 50%, which translates to significant computational savings. This implies that WMLES has the potential to treat natural convection cases at higher Ra than DNS and WRLES can. For all simulations presented in this work, the time step is determined via the CFL condition with the Courant number set to 0.05. It is also worth adding that since the grid in WMLES is coarser, the average time step is also larger than in WRLES, which results in even shorter computation times.

Table 2 Properties of the computational grids used in the comparative studies. N is the number of grid cells in each direction, $\Delta\hat{x}_{\mathrm{min}}$ is the minimum grid spacing (near the boundaries), and $\Delta\hat{x}_{\mathrm{max}}$ is the maximum grid spacing (at the centre of the domain)

		Box			Cavity		
Ra	simulation	N	$\Delta\hat{x}_{\mathrm{min}}$	$\Delta\hat{x}_{\mathrm{max}}$	N	$\Delta\hat{x}_{\mathrm{min}}$	$\Delta\hat{x}_{\mathrm{max}}$
1.35×10^8	WRLES	62	1.86×10^{-3}	3.7×10^{-2}	68	1.22×10^{-3}	3.66×10^{-2}
	WMLES	50	5.81×10^{-3}	3.48×10^{-2}	48	6.41×10^{-3}	3.56×10^{-2}
10^9	WRLES	118	8.47×10^{-4}	1.98×10^{-2}	132	5.91×10^{-4}	1.88×10^{-2}
	WMLES	92	2.72×10^{-3}	1.96×10^{-2}	88	3.48×10^{-3}	1.91×10^{-2}
	Kader	100	1.804×10^{-3}	1.99×10^{-2}	-	-	-

As mentioned above, the working medium in our study is liquid water. In all cases presented here, the reference temperature and pressure have been set to $T_{\mathrm{ref}} = 359.3$ K and $p_{\mathrm{ref}} = 1$ bar, respectively. The physical parameters of water at these conditions are given in Table 3.

Table 3 Physical parameters of liquid water at the reference conditions $T_{\mathrm{ref}} = 359.3$ K and $p_{\mathrm{ref}} = 1$ bar

Pr	ρ_{ref} [kg/m^3]	μ_{ref} [kg/m s]	$c_{p,\mathrm{ref}}$ [J/kg K]	λ_{ref} [W/m K]	β_{ref} [1/K]	α_{ref} [m^2/s]
2.06	967.86	3.29×10^{-4}	4201.2	0.67	6.7×10^{-4}	1.64×10^{-7}

Concerning the boundary conditions at the top boundary, we prescribe a zero-slip condition for RBC in a box, and a free-slip condition for RBC in a cavity. Accordingly, for the case of a cavity and in the absence of a top hydrodynamic layer, we do not employ any wall model for the momentum equation at the top boundary. The bottom wall is maintained at T_h and the top one at T_c, with $T_\mathrm{h} > T_\mathrm{c}$. Whereas all lateral walls are adiabatically isolated. Initially, the fluid is assumed to be at rest and a linear temperature profile is prescribed in the (vertical) y-direction.

The simulation parameters and estimated thicknesses of the boundary layers for the various cases of our comparative study are provided in Table 4. The estimates for the thicknesses of the hydrodynamic and thermal boundary layers are computed from equations (30) and (31), respectively.

Table 4 Simulation parameters for the comparative studies and estimated thicknesses of the boundary layers from equations (30) and (31)

	Box				Cavity			
Ra	L [m]	ΔT [K]	$\hat{\delta}_u^{\mathrm{es}}$	$\hat{\delta}_\theta^{\mathrm{es}}$	L [m]	ΔT [K]	$\hat{\delta}_u^{\mathrm{es}}$	$\hat{\delta}_\theta^{\mathrm{es}}$
1.35×10^8	0.045	12.7	0.0159	0.0124	0.045	12.7	0.0128	0.01
10^9	0.088	12.7	0.0085	0.0067	0.1	8.5	0.007	0.0055

Our numerical tests showed that in all cases the flow becomes statistically stationary after 300 t_ff or earlier. Accordingly, the simulations of all cases are first run for 300 t_ff to wash out all transient effects before we start taking time averages (Stevens et al., 2010). Subsequently, the simulations are run for an additional period of 250 t_ff, during which we compute time averages. For the range of Rayleigh numbers considered herein, this period is deemed sufficient for computing converged time-averaged quantities, in the sense that any further increase of the averaging period will not lead to modified time-averaged quantities. Actually, according to earlier DNS results (Stevens et al., 2010), and at the range of Rayleigh numbers of interest ($\mathrm{Ra} = 2\times10^{10}$), a time-averaging period of 100 t_ff is sufficient to obtain converged time statistics once the flow becomes statistically stationary. For greater confidence, in our simulations we have increased the time interval of the statistics to 250 t_ff.

5 Numerical Results

In this section, we first compare the results of the WMLES using the thermal boundary models described in section 3. First, we analyse and compare results for RBC in a box, and then for RBC in a cubic cavity. Subsequently, we present WMLES results of turbulent convection at a higher Rayleigh number, $Ra = 5\times10^9$, using the thermal boundary model that performed the.

Concerning terminology and notation, the mean of a given quantity is defined as its average in time and along the horizontal (x and z) directions and is denoted by brackets. For example, the mean of a generic quantity ϕ is denoted by $\langle\phi\rangle$. The fluctuating component of ϕ is denoted by ϕ', so that $\phi = \langle\phi\rangle + \phi'$. Also the root mean square of the fluctuations of ϕ is denoted by $\phi_\mathrm{rms} = \sqrt{\phi'\phi'}$.

The profiles shown in the following section depict time and area-averaged (along the x and z-directions) quantities along the y-direction.

5.1 Comparative study of natural convection in a box

First, we compare the numerical predictions for the mean temperature, obtained with the four different thermal models under consideration. To this end, we introduce the normalized temperature Θ,

$$\Theta \;=\; \frac{T - T_{\rm ref}}{\Delta T}\,. \tag{34}$$

In Figures 1a and 1b we present plots of the profiles of the mean normalized temperature, $\langle\Theta\rangle$, for the two different Rayleigh numbers mentioned above, $Ra = 1.35{\times}10^8$ and $Ra = 10^9$. In these figures, we observe that the profiles obtained with the RA, KC1 and KC2 models are very close to those obtained with WRLES. This is true for both the near-wall regions and the bulk of the computational domain. On the other hand, the profile obtained with the Kader model is shifted to the left. This shift is more pronounced at $Ra = 1.35{\times}10^8$. The shift is smaller at $Ra = 10^9$ but this improvement is explained by the fact that for this particular case we had to increase the grid resolution in the simulations with the Kader model.

It is also worth adding that the profiles of $\langle\Theta\rangle$ are not perfectly symmetric with respect to the midheight plane, *i*.e. the plane $y/L = 0.5$. This is attributed to the dependence of the transport properties of the fluid, μ and λ, on the temperature (Sugiyama et al., 2009; Hay and Papalexandris, 2019). This means that the slight asymmetry is a non-Oberbeck-Boussinesq effect; indeed, the Oberbeck-Boussinesq approximation has not been invoked in the governing system of equations (1)-(3).

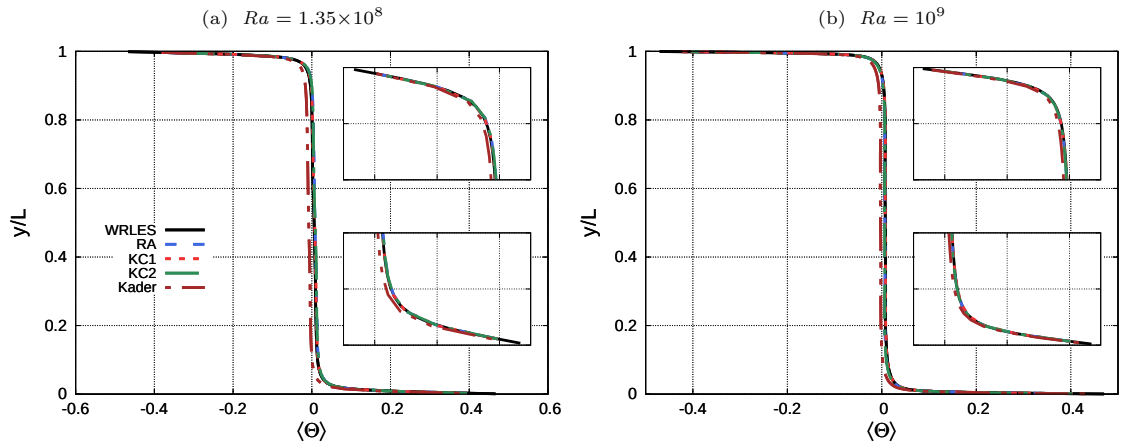


Fig. 1 RBC in a box: profiles of mean normalized temperature $\langle\Theta\rangle$ from WMLES with different thermal boundary models and from WRLES. The inserts show the zoom of these profiles near the top and bottom boundaries respectively. (a) $Ra = 1.35{\times}10^8$; (b) $Ra = 10^9$

We proceed to examine the predictions for the profile of the (local) Nusselt number along the y-direction, $Nu(y)$. This quantity is defined as the sum of convective, diffusive and turbulent (subgrid) contributions as follows,

$$Nu(y) \;=\; \underbrace{\sqrt{RaPr}\,\langle\hat{\rho}\hat{v}\Theta\rangle}_{Nu_{\rm conv}} - \underbrace{\langle\hat{\lambda}\frac{\partial\Theta}{\partial\hat{y}}\rangle}_{Nu_{\rm diff}} - \underbrace{\langle\hat{\lambda}_t\frac{\partial\Theta}{\partial\hat{y}}\rangle}_{Nu_{\rm turb}}\,. \tag{35}$$

Accordingly, the diffusive contribution of $Nu(y)$ involves the resolved dimensionless conductivity $\hat{\lambda}$, while the turbulent one involves the dimensionless turbulent conductivity $\hat{\lambda}_t$.

In Figures 2a and 2b, we present the profiles of $Nu(y)$ computed via equation (35). For a fully developed flow, $Nu(y)$ is expected to be constant. Nonetheless, the numerical profiles exhibit an overshoot and subsequently an undershoot adjacent to each boundary, $y/L = 0$ and $y/L = 1$, and a mild fluctuation in bulk. Such overshoot is a well-known feature of numerical simulations of natural convection due to high temperature gradients at the walls (Yilmaz, 2020). Still, the overshoots in WMLES are considerably higher than in WRLES. This suggests that the grid resolution near the boundaries and the value of the exchange location are linked to the magnitude of these overshoots and undershoots. Compared to boundary-layer resolving grids, wall models necessarily introduce additional errors and the value of the exchange location has to be selected to minimise them (Kahraman and Larsson, 2022). The exchange location is set based on the hydrodynamic boundary layer thickness. The same exchange location has been used for both the velocity wall model and the thermal boundary model. Nevertheless, the hydrodynamic layer is thicker than the thermal one. Accordingly, the exchange location for the thermal model could also be set in a different manner so as to try to minimize the those overshoots and undershoots of $Nu(y)$.

We further note that the fluctuation of $Nu(y)$ in the bulk is a numerical artifact and arises because an LES does not resolve all turbulent structures. In other words, this deviation is due to the coarseness of the LES grids in the bulk and is not necessarily related to the thermal boundary models. This is supported by the fact that, according to Figures 2a and 2b, in the bulk the fluctuations of all WMLES profiles are very similar to that of the WRLES profile.

Overall, all WMLES profiles are quite close to their WRLES counterpart. In terms of comparisons, the profile computed with the KC1 model is the closest to the WRLES profile; whereas the profiles of the Kader and KC2 models exhibit the largest deviation. Once again, at $Ra = 10^9$ the predictions with the Kader model are improved but this is due to the higher grid resolution employed with this model at this Ra.

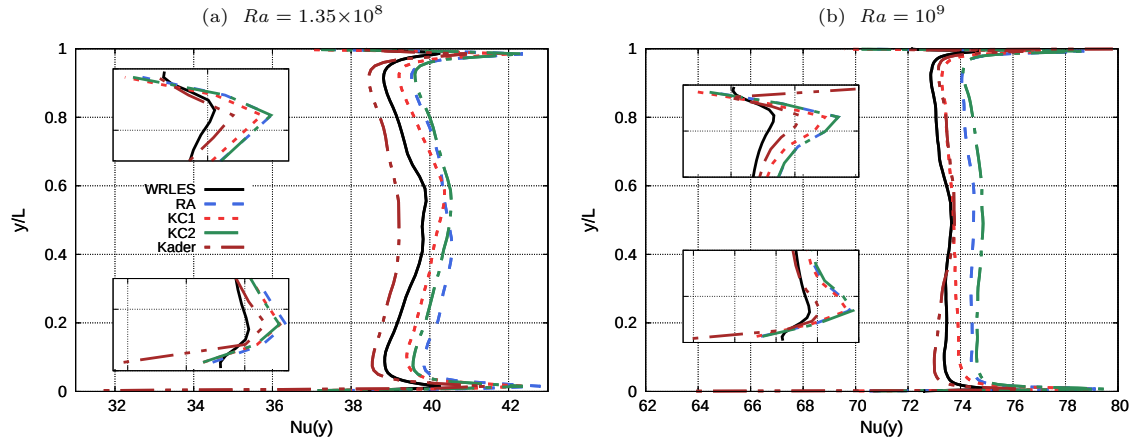


Fig. 2 RBC in a box: profiles of the (local) Nusselt number $Nu(y)$ from WMLES with different thermal boundary models and from WRLES. The inserts show the zoom of these profiles near the top and bottom boundaries respectively. (a) $Ra = 1.35\times10^8$; (b) $Ra = 10^9$

By taking the average of $Nu(y)$, while excluding the near-boundary numerical overshoots, we can get an estimate of the (global) Nusselt number, Nu. In Table 5, we provide the numerical predictions for Nu from the four WMLES and from the WRLES. For comparison purposes, in the same table, we have included the values of Nu based on the correlation (28). The average values $Nu(y)$ computed

in this manner is intended only to provide an estimate of the error in the computation of Nu that is attributed to LES. The near-boundary overshoots are also present in DNS and, therefore, are not due to LES. This is why these overshoots have been not takes into account when computing the average.

In all cases, the discrepancy from the correlation (28) is less than 4%. It is interesting to observe that the predictions of WMLES with the RA, KC1 and KC2 models are slightly closer to the correlation than the result of WRLES. This, however, does not necessarily imply that WMLES is more accurate than WRLES because correlations such as equation (28) also entail errors and their accuracy has certain limits. On the other hand, from the values listed in this table, we readily conclude that the Kader model yields less accurate estimates.

Table 5 RBC in a box: Nusselt number obtained via WMLES and WRLES. The listed values are the averages of the computed profiles of $Nu(y)$. The second column shows the values based on the correlation (28)

Ra	Corr. (28)	WRLES	RA	KC-1	KC-2	Kader
1.35×10^8	40.3	39.2	40.1	39.7	40	38.8
10^9	74.9	73.3	74.3	73.7	74.6	73.3

Further insight into the errors induced by the thermal boundary models can be obtained upon examination of the turbulent contribution to the Nusselt number, Nu_{turb}, the profiles of which are plotted in Figures 3a and 3b. We can observe that the Kader model predicts a negative value at the bottom wall and a positive value at the top one. These spurious values certainly contribute to the numerical errors associated with this model. On the contrary, the other thermal boundary models predict zero values for Nu_{turb} at the walls, which is the correct behaviour. It is also interesting to observe that in the bulk, the values of Nu_{turb} are very small and practically constant. Moreover, all WMLES profiles of Nu_{turb} in the bulk coincide with the WRLES profile.

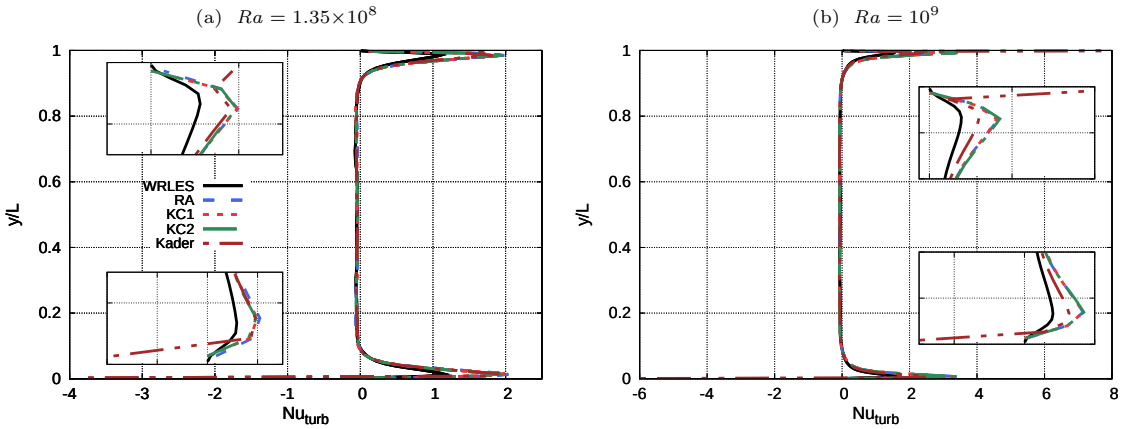


Fig. 3 RBC in a box: profiles of the turbulent contribution of the (local) Nusselt number Nu_{turb} from WMLES with different thermal boundary models and from WRLES. The inserts show the zoom of these profiles near the top and bottom boundaries respectively. (a) $Ra = 1.35\times10^8$; (b) $Ra = 10^9$

Next, we compare the predictions for certain important second-order flow statistics. In Figures 4a and 4b, we have plotted the profiles for the root-mean-square (rms) of the temperature fluctuations,

Θ_{rms}. As expected, the rms values rise rapidly off the walls and peak very close to them. These peaks are located at the edges of the thermal boundary layers. Away from these peaks, the values of Θ_{rms} drop until they reach a minimum at midheight. In terms of comparisons, the profiles obtained with the four different thermal boundary models are practically identical and very close to the profile computed via WRLES, both in the near-wall regions and in the bulk.

By taking the thickness of the thermal boundary layer, $\hat{\delta}_\theta$, to be equal to the distance of the peak of Θ_{rms} from the wall, we can compare the numerical predictions for it with the estimates from equation (31). These comparisons are summarized in Table 6. For RBC in a box at $Ra = 1.35{\times}10^8$, the predictions of WMLES and WRLES for $\hat{\delta}_\theta$ coincide and are equal to 0.95 of the estimate of equation (31). Whereas for $Ra = 10^9$, the prediction of WRLES is slightly more accurate than that of WMLES; 0.99 and 1.04 respectively of the estimate of equation (31). We may therefore infer that the grid resolution near the wall is satisfactory for both WRLES and WMLES.

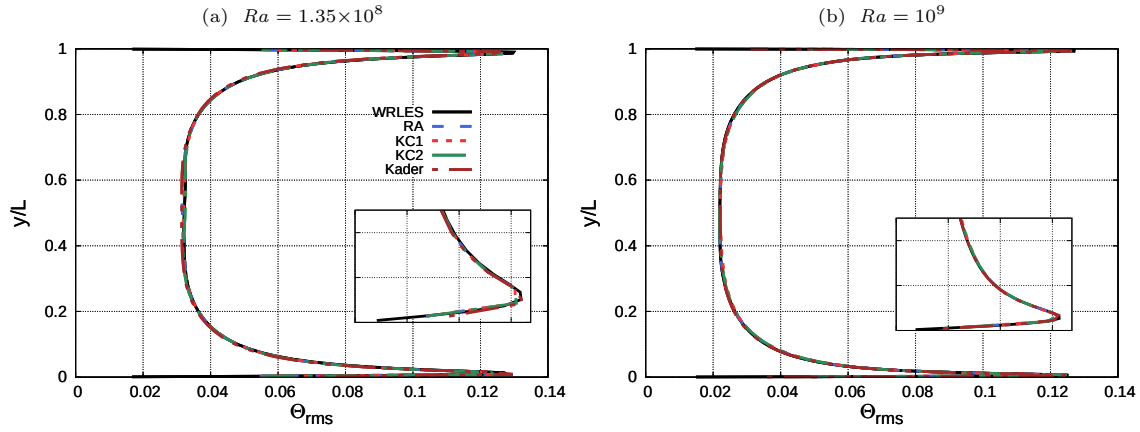


Fig. 4 RBC in a box: profiles of the rms of normalized temperature fluctuations Θ_{rms} from WMLES with different thermal boundary models and from WRLES. The inserts show the zoom of these profiles near the bottom boundary. (a) $Ra = 1.35{\times}10^8$; (b) $Ra = 10^9$

In Figures 5a and 5b, we have plotted the profiles of the rms of the fluctuations of the in-plane and vertical velocity components, respectively, at $Ra = 1.35{\times}10^8$. The rms of the horizontal in-plane velocity rms is denoted by $\overline{u}_{\text{rms}}$ and defined by $\overline{u}_{\text{rms}} = \sqrt{u'u' + w'w'}$. In a subsequent section, we will compare velocity rms at different Rayleigh numbers; therefore these quantities have been made dimensionless by the ratio α_{ref}/L. From these plots, we can observe that overall the profiles obtained with all thermal boundary models agree quite well with those of WRLES. In particular, both the amplitude and location of the peak of $\overline{u}_{\text{rms}}$ are well predicted. In the bulk, there are some small discrepancies, with the Kader model exhibiting the largest deviation from the WRLES. Also, the profiles of v_{rms} show very good agreement with those obtained via WRLES, albeit with some slight deviations at midheight. For the case of $Ra = 10^9$, the rms profiles have the same characteristics. Accordingly, on the purposes of the economy of space, their plots are not shown herein.

The thickness of the hydrodynamic boundary layers is assumed to be equal to the distance of the peak of $\overline{u}_{\text{rms}}$ from the respective wall. The numerical predictions for the boundary-layer thickness $\hat{\delta}_u$ obtained in this manner are compared with the estimates obtained from equation (30) in Table 6. From the values listed therein, we can infer that the comparison between LES predictions and estimates of equation (30) is not as good as in the thermal boundary layers. More specifically, both

the WMLES and WRLES predictions differ by approximately 20% from the estimates of equation (30).

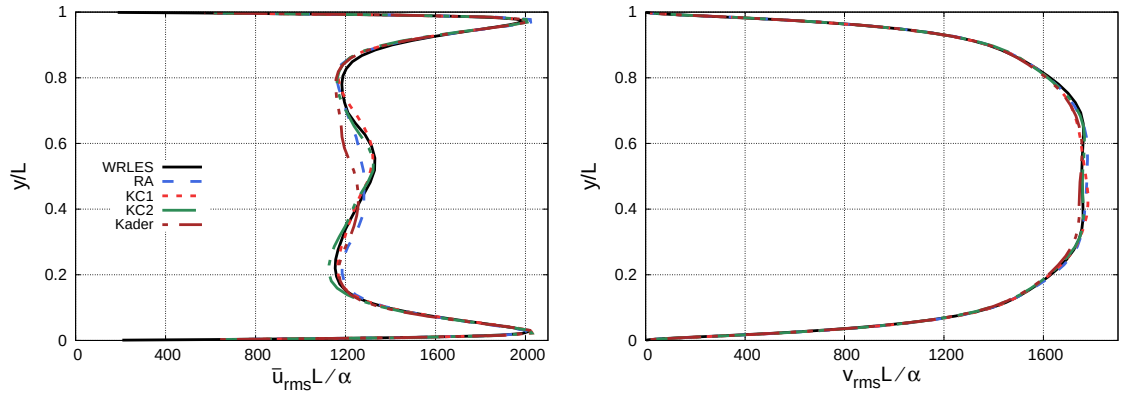


Fig. 5 RBC in a box: profiles of the rms of normalized velocity fluctuations at $Ra = 1.35\times10^8$ from WMLES with different thermal boundary models and from WRLES. (a) rms of the in-plane velocity fluctuation $\overline{u}_{\rm rms}$; (b) rms of vertical velocity fluctuation $v_{\rm rms}$

In summary, among the four thermal boundary models considered herein, the RA, KC1 and KC2 models provided quite accurate results, with the performance of KC1 and RA being slightly superior to that of KC2. On the other hand, the Kader model did not perform particularly well; it produced comparatively large errors in the near-boundary value of λ_t and required a finer grid than the other models.

Table 6 RBC in a box: comparison of the predictions for the thicknesses of the hydrodynamic and thermal boundary layers. The subscripts wr and wm denote predictions from WRLES and WMLES, respectively. The predicted values have been normalized by the estimates $\hat{\delta}_u^{\rm es}$ and $\hat{\delta}_\theta^{\rm es}$ obtained from equations (30) and (31) respectively

Ra	$\hat{\delta}_u^{\rm wr}/\hat{\delta}_u^{\rm es}$	$\hat{\delta}_u^{\rm wm}/\hat{\delta}_u^{\rm es}$	$\hat{\delta}_\theta^{\rm wr}/\hat{\delta}_\theta^{\rm es}$	$\hat{\delta}_\theta^{\rm wm}/\hat{\delta}_\theta^{\rm es}$
1.35×10^8	0.83	0.78	0.95	0.95
10^9	0.81	0.83	0.99	1.04

5.2 Comparative study of natural convection in a cavity

In this section, we consider turbulent natural convection in a cavity and present WMLES results obtained with the various thermal boundary models. As mentioned in section 3, the Kader model cannot be applied in free-slip boundaries. Therefore, we assess the efficacy of the other three models: RA, KC1 and KC2.

Figures 6a and 6b show profiles of the mean normalized temperature $\langle\Theta\rangle$ at $Ra = 1.35\times10^8$ and $Ra = 10^9$, respectively. Overall, the WMLES profiles are satisfactorily close to the WRLES ones. For RBC in a cavity, we expect that the profile of $\langle\Theta\rangle$ to be shifted to the left (Hay and Papalexandris, 2019). This is because the absence of shear stress on top enhances convective motions and turbulent mixing which, in turn, decreases the temperature in the bulk to values that are closer to that of the top cold boundary $T_{\rm c}$. The profiles of $\langle\Theta\rangle$ obtained with WRLES exhibit such a small shift to the left. The profiles predicted with the RA model also exhibit the expected shift to the left at both

Rayleigh numbers and almost match the WRLES ones. On the other hand, the profiles predicted with the KC1 and KC2 models exhibit a small shift to the right with respect to the WRLES profile. In other words, they predict somewhat higher temperatures in the bulk. This means that the RA model gave more accurate predictions for $\langle\Theta\rangle$ than the KC1 and KC2 models did.

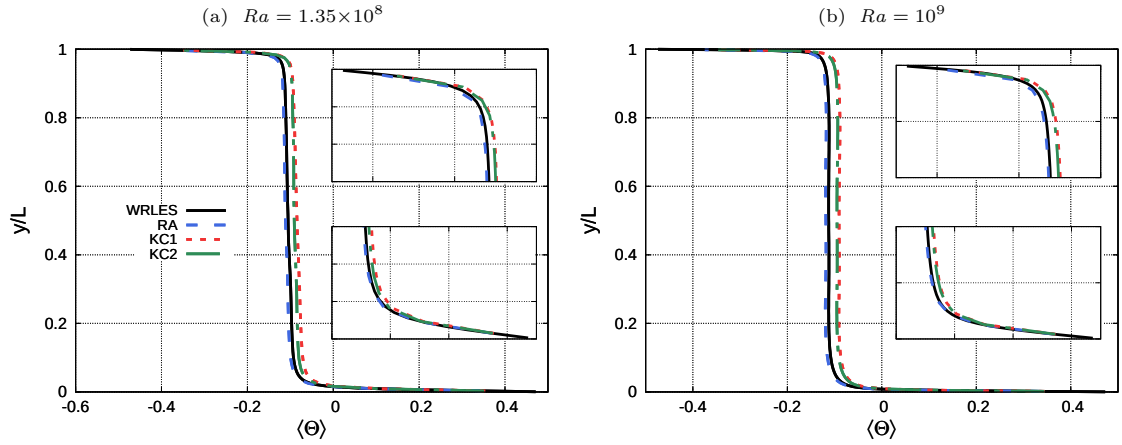


Fig. 6 RBC in a cavity: profiles of mean normalized temperature $\langle\Theta\rangle$ from WMLES with different thermal boundary models and from WRLES. The inserts show the zoom of these profiles near the top and bottom boundaries respectively. (a) $Ra = 1.35\times10^8$; (b) $Ra = 10^9$

Next, in Figures 7a and 7b we present the profiles of the (local) Nusselt number $Nu(y)$. The computed profiles exhibit an overshoot close to the boundaries and a small variation in the bulk. As mentioned in the previous section, both of these features are numerical artifacts. Besides that, the best match to the WRLES profiles were those obtained with the KC2 model, with the KC1 model coming second in accuracy. On the other hand, concerning $Nu(y)$, the RA model was comparatively less accurate. More specifically, it overestimated $Nu(y)$ by nearly 8% at $Ra = 1.35\times10^8$ and by 12% at $Ra = 10^9$.

The predictions for the (global) Nusselt number Nu are provided in Table 7. In the same table, we have also listed the values obtained by the correlation (29). We observe that WRLES predicted higher values of Nu than those of equation (29). Moreover, the discrepancy between them appears to increase with the Rayleigh number. It must be noted, however, that the $Nu - Ra$ correlation (29) takes into account evaporation across the top free-slip plane. Moreover, this correlation was computed from direct numerical simulations at lower Rayleigh numbers. These two factors are expected to contribute to the observed discrepancy between WRLES and correlation (29). With respect to the thermal boundary models under consideration, and based on the values in Table 7, we reaffirm that the most accurate predictions were obtained with the KC2 model and the least accurate ones with the RA model.

In Figures 8a and 8b, we have plotted the profiles of the turbulent contribution to the Nusselt number Nu_{turb} given in equation (35). It is interesting to observe that close to the top free-slip boundary, the values obtained with the RA model are larger than those with the other models. Furthermore, the RA model results in a much higher overshoot adjacent to this boundary. In other words, the RA model gives less accurate predictions for Nu_{turb} than the other models do. This can be explained as follows; since the shear stresses are zero at the top boundary, the turbulent viscosity μ_t is higher near the top than near the bottom. Further, according to the RA model in equation

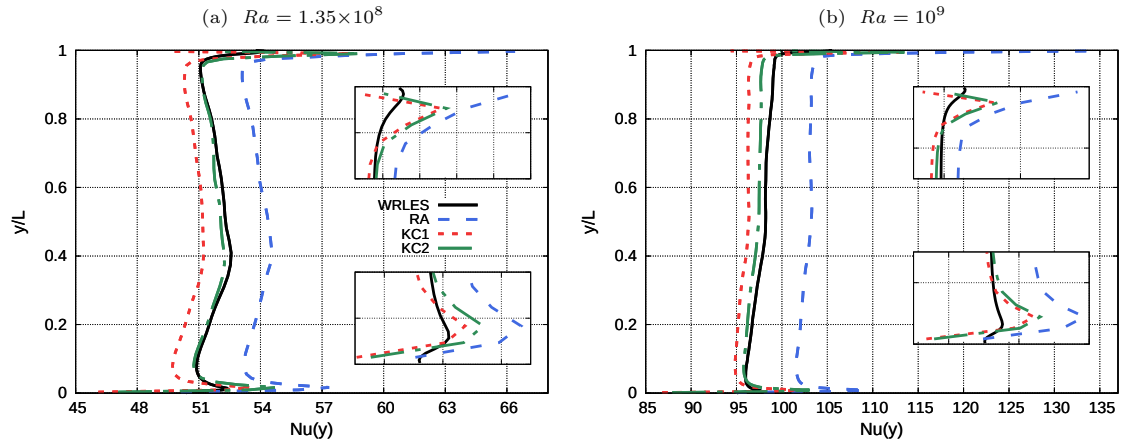


Fig. 7 RBC in a cavity: profiles of the (local) Nusselt number $Nu(y)$ from WMLES with different thermal boundary models and from WRLES. The inserts show the zoom of these profiles near the top and bottom boundaries respectively. (a) $Ra = 1.35\times10^8$; (b) $Ra = 10^9$

Table 7 RBC in a cavity: Nusselt number obtained via WMLES and WRLES. The listed values are the averages of the computed profiles of $Nu(y)$; the second column shows the values based on the correlation (29)

Ra	Corr. (29)	WRLES	RA	KC1	KC2
1.35×10^8	49.8	51.5	53.7	50.5	51.5
10^9	91.1	97.7	102.7	95.8	97

(17), the turbulent conductivity λ_t scales linearly with the turbulent viscosity: $\lambda_t \sim \mu_t$. Whereas in the KC1 and KC2 models, relations (18) and (19) respectively, it scales with the inverse of the turbulent viscosity: $\lambda_t \sim \frac{1}{\mu_t}$. As a result, the predictions of the RA model for λ_t at the top are much higher than those of the other models, which causes the observed overshoots.

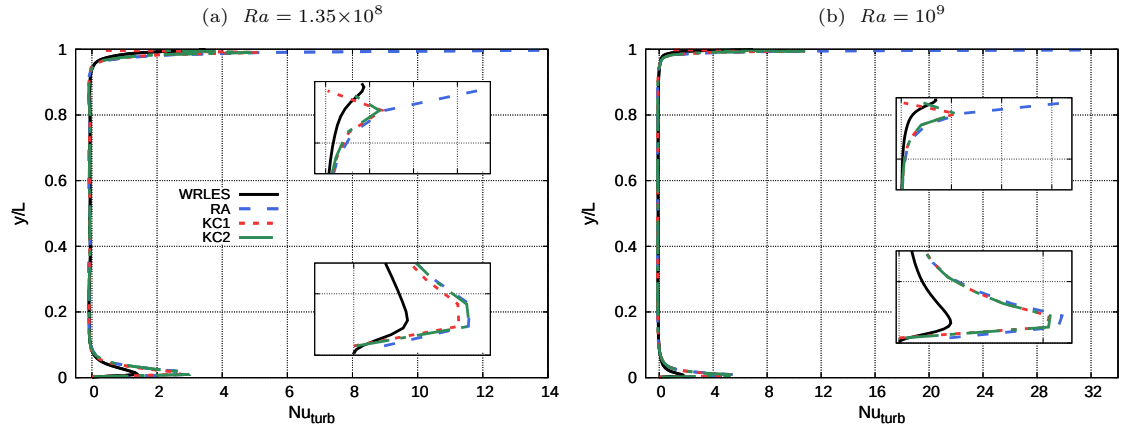


Fig. 8 RBC in a cavity: profiles of the turbulent contribution of the Nusselt number Nu_{turb} from WMLES with different thermal boundary models and from WRLES. The inserts show the zoom of these profiles near the top and bottom boundaries respectively. (a) $Ra = 1.35\times10^8$; (b) $Ra = 10^9$

This can be further corroborated by the plots of the profiles of the turbulent conductivity λ_t which are shown in Figures 9a and 9b. Compared to WRLES, the RA model overestimates λ_t at

the free-slip boundary by a factor of 4.9 at $Ra = 1.35\times10^8$, and by a factor of 5.6 at $Ra = 10^9$. By contrast, KC2 predicts a small positive value for λ_t at the top which is almost equal to the value of the WRLES. Whereas the KC1 model predicts a zero value for λ_t.

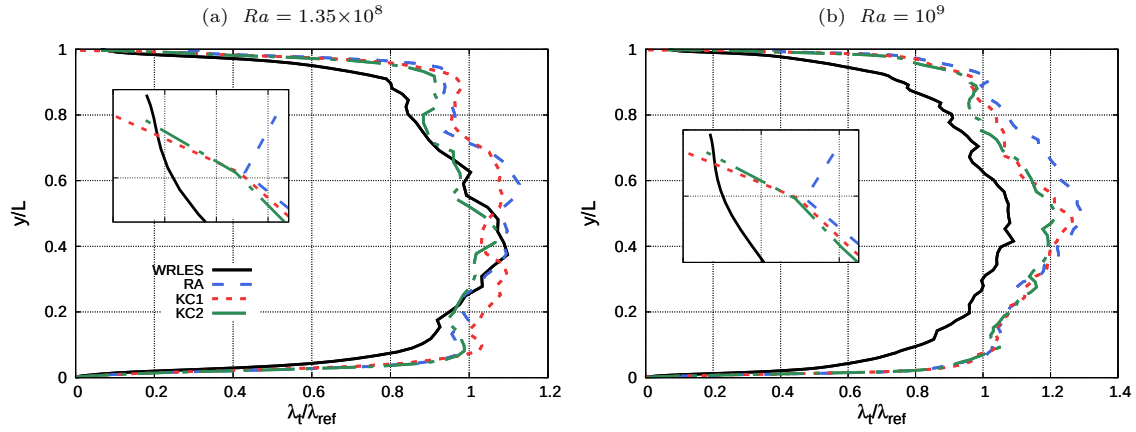


Fig. 9 RBC in a cavity: profiles of the turbulent heat conductivity λ_t from WMLES with different thermal boundary models and from WRLES. The inserts show the zoom of these profiles near the top boundary. (a) $Ra = 1.35\times10^8$; (b) $Ra = 10^9$

The computed profiles of the rms of the temperature fluctuations are provided in Figures 10a and 10b. The most noticeable feature is that these profiles are no longer symmetric with respect to the midheight. More specifically, the peak of $\Theta_{\rm rms}$ near the bottom boundary is much higher than that near the top. This is attributed to the absence of a hydrodynamic boundary layer on top which results in higher turbulent intensity and more efficient turbulent mixing and, consequently, smaller thermal fluctuations. Also, from these figures, we can infer that the thermal boundary models yielded very similar profiles for $\Theta_{\rm rms}$ that are also very close to those of WRLES. It is especially interesting to observe that the predictions of all WMLES and the WRLES for the amplitudes and locations of the peaks of $\Theta_{\rm rms}$ are very close to one another.

In Table 8 we provide results for the thicknesses of the hydrodynamic and thermal boundary layers at the bottom and top boundaries. According to it, the predictions of WMLES and WRLES for the thickness of the top thermal layer match the values obtained from the correlation (31). With regard to the bottom thermal layer, the predictions of WMLES show a maximum discrepancy of 6% from the values obtained from equation (31). Whereas, WRLES gives a very accurate prediction at $Ra = 10^9$ but shows a discrepancy of 13% at $Ra = 1.35\times10^8$. Also, with regard to the bottom hydrodynamic layer, the predictions of both WMLES and WRLES are quite close, with a maximum deviation of 7% and 8%, respectively.

Table 8 RBC in a cavity: comparison of the predictions for the thicknesses of the hydrodynamic and thermal boundary layers at the bottom and top boundaries; the notation is the same as in Table 6

			Bottom		Top	
Ra	$\hat\delta_u^{\rm wr}/\hat\delta_u^{\rm es}$	$\hat\delta_u^{\rm wm}/\hat\delta_u^{\rm es}$	$\hat\delta_\theta^{\rm wr}/\hat\delta_\theta^{\rm es}$	$\hat\delta_\theta^{\rm wm}/\hat\delta_\theta^{\rm es}$	$\hat\delta_\theta^{\rm wr}/\hat\delta_\theta^{\rm es}$	$\hat\delta_\theta^{\rm wm}/\hat\delta_\theta^{\rm es}$
1.35×10^8	0.92	0.98	1.13	0.94	1.001	1.00
10^9	0.92	0.93	1.00	0.98	1.00	1.00

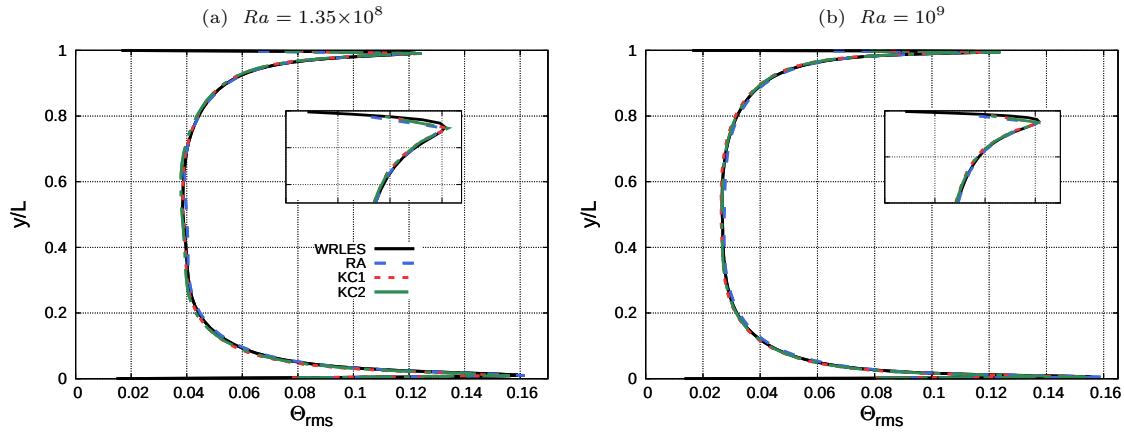


Fig. 10 RBC in a cavity: profiles of the rms of normalized temperature fluctuations $\Theta_{\rm rms}$ from WMLES with different thermal boundary models and from WRLES. The inserts show the zoom of these profiles near the top boundary. (a) $Ra = 1.35\times10^8$; (b) $Ra = 10^9$

For the case of $Ra = 1.35\times10^8$, in Figures 11a and 11b, we have plotted the profiles of the rms fluctuations of the in-plane $\overline{u}_{\rm rms}$ and vertical $v_{\rm rms}$ velocity components, respectively. Overall, the shapes of these profiles are very close to those predicted by the WRLES of Hay et al. (2021) at lower Rayleigh numbers. Their most interesting feature is that due to the absence of a top hydrodynamic layer, the values of $\overline{u}_{\rm rms}$ do not vanish at the top boundary but, instead, they are maximized. With regard to WMLES, the predictions of all thermal boundary models are satisfactorily accurate. In terms of comparisons, the $\overline{u}_{\rm rms}$ profile of the KC1 model is the closest to the one of WRLES, followed by the profile of the RA model. Whereas, the $\overline{u}_{\rm rms}$ profile of the KC2 model exhibits the largest deviations from the WRLES results. On the other hand, the $v_{\rm rms}$ profiles obtained with KC1 and KC2 are very close to the WRLES results while the profile of RA slightly overestimated the peak value in the bulk. For the case of RBC in a cavity at $Ra = 10^9$, the computed profiles exhibit the same characteristics and have not been included herein for purposes of the economy of space.

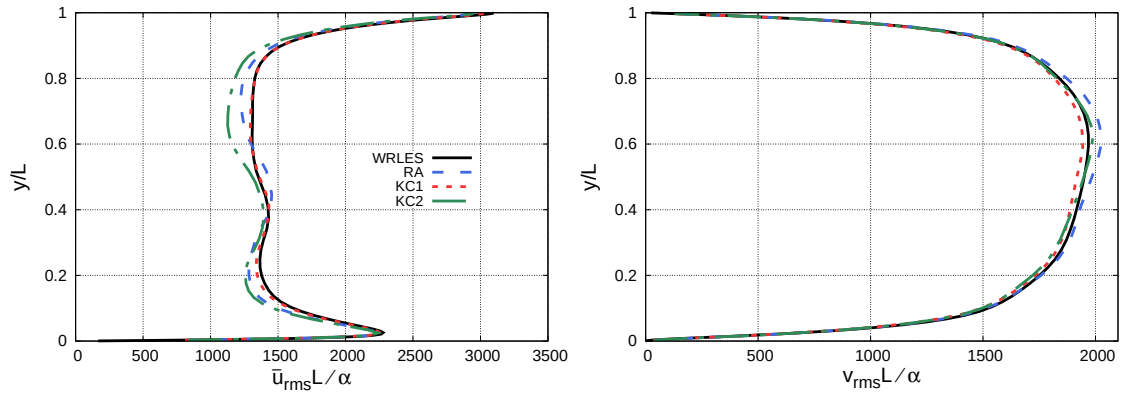


Fig. 11 RBC in a cavity: profiles of the rms of normalized velocity fluctuations at $Ra = 1.35\times10^8$ from WMLES with different thermal boundary models and from WRLES. (a) rms of the in-plane velocity fluctuation $\overline{u}_{\rm rms}$; (b) rms of vertical velocity fluctuation $v_{\rm rms}$

In summary, even though the RA model gave slightly more accurate predictions for $\langle\Theta\rangle$ than the other two models, its predictions for λ_t near the free-slip boundary were not accurate. This introduced a noticeable error in the predictions of the Nusselt number. Globally, the KC1 and KC2 models gave

more accurate predictions than the RA model did. The KC1 model slightly outperformed KC2 in the predictions of the velocity rms, while the opposite was true for the predictions of the Nusselt number. Nonetheless, the overall accuracy of the KC1 and KC2 models was comparable.

5.3 WMLES for natural convection at $Ra = 5\times10^9$

In this section, we present results for WMLES of natural convection in a box and in a cavity at a higher Reynolds number, namely $Ra = 5\times10^9$. For our simulations, we have selected the KC1 model which is given by equation (18). This choice is motivated by two reasons. The first one is that, according to our comparative studies in sections 5.1 and 5.2 above, the KC1 model gave quite accurate results for both configurations, box and cavity. The second reason is that the implementation of this model is straightforward.

The objectives of this numerical study are to explore further the robustness of the KC1 model and to gain physical insight into the turbulent convection of water at higher Rayleigh numbers. It is worth reiterating that numerical results for RBC of fluids with $Pr > 1$ at high Ra are currently unavailable. Moreover, WRLES at $Ra = 5\times10^9$ is computationally quite expensive. For this reason, we resort to WMLES.

As in our comparative study, the computational domain is a cube. The domain height, grid resolution, maximum and minimum grid spacing, temperature difference, and estimated boundary layer thicknesses are provided in Table 9 below. The estimates for the thicknesses of the hydrodynamic and thermal boundary layers have been computed from equations (30) and (31), respectively.

Table 9 at $Ra = 5\times10^9$: grid properties and simulation parameters for WMLES; the notation is the same as in Table 2

	L [m]	N	$\Delta\hat{x}_{\min}$	$\Delta\hat{x}_{\max}$	ΔT [K]	$\hat{\delta}_u^{\text{es}}$	$\hat{\delta}_\theta^{\text{es}}$
Box	0.15	150	0.0017	0.0118	12.6	0.0052	0.0041
Cavity	0.15	182	0.0011	0.0107	12.6	0.0043	0.0034

In figures 12a and 12b, we provide contour plots of time-averaged streamlines coloured by the mean temperature for the two configurations, box and cavity, respectively. We can observe that the flow structure is fairly similar in both cases, characterized by an ascending hot current in one corner and a descending cold one at the opposite corner. Further, we can discern the impingement points of the hot plumes at the top boundary. These features imply that these currents are part of a large convective structure, the so-called Large Scale Circulation (LSC). The LSC is the most characteristic feature of natural convection at weak and moderate turbulence intensities. It is aligned in one diagonal plane and can reorient itself either by changing the plane of alignment or direction of rotation (Foroozani et al., 2017; Marichal and Papalexandris, 2022).

From the same figures, we can also confirm that in RBC in a cavity, the temperature variations in the bulk are less pronounced than in RBC in a box. Furthermore, in the case of a cavity, the temperatures in the bulk are comparatively lower, *i.e.* they are shifted towards that of the top boundary. As mentioned above, this is attributed to the absence of a hydrodynamic layer on top which increases the turbulence intensity and enhances turbulent mixing.

In Figures 13a and 13b, we have plotted the profiles of the mean normalized temperature $\langle\Theta\rangle$ for RBC in a box and in a cavity, respectively. In these, we have included the profiles for all three

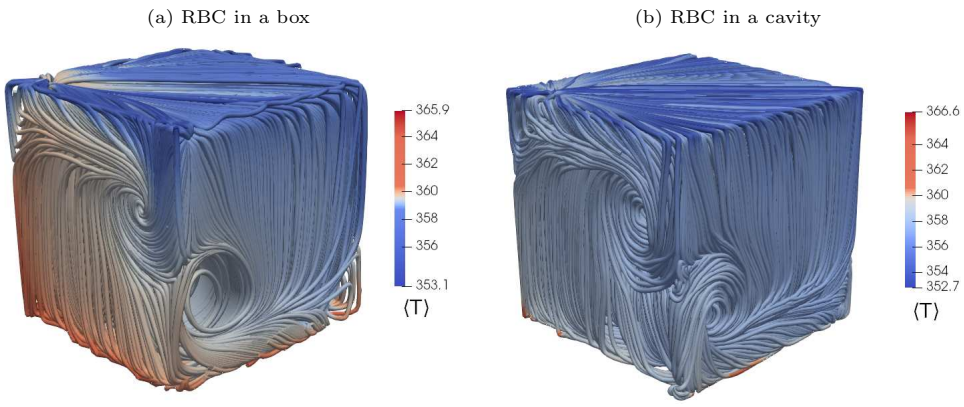


Fig. 12 RBC at $Ra = 5{\times}10^9$: time-averaged streamlines colored by the mean temperature $\langle T \rangle$; (a) box; (b) cavity

Rayleigh numbers considered in our study. With regard to RBC in a box, we can observe that the $\langle \Theta \rangle$ profiles in the bulk are almost identical. Further, the profiles are almost but not fully symmetrical due to the variations of the transport parameters with the temperature. The main effect of increasing Ra is that the slope of $\langle \Theta \rangle$ near the boundaries increases and that the thickness of the hydrodynamic boundary layer becomes smaller, as expected.

On the other hand, for RBC in a cavity, the effect of Ra is more pronounced. More specifically, as Ra gets higher, the profile of $\langle \Theta \rangle$ shifts to the left, *i.e.* towards the temperature of the top cold boundary. At the same time, the slope of $\langle \Theta \rangle$ near the boundaries is as well increasing, but with a less pronounced effect at the free-slip boundary. Both features are due to the fact that higher Ra results in stronger convective motions and increased turbulent mixing, especially in the upper part of the domain.

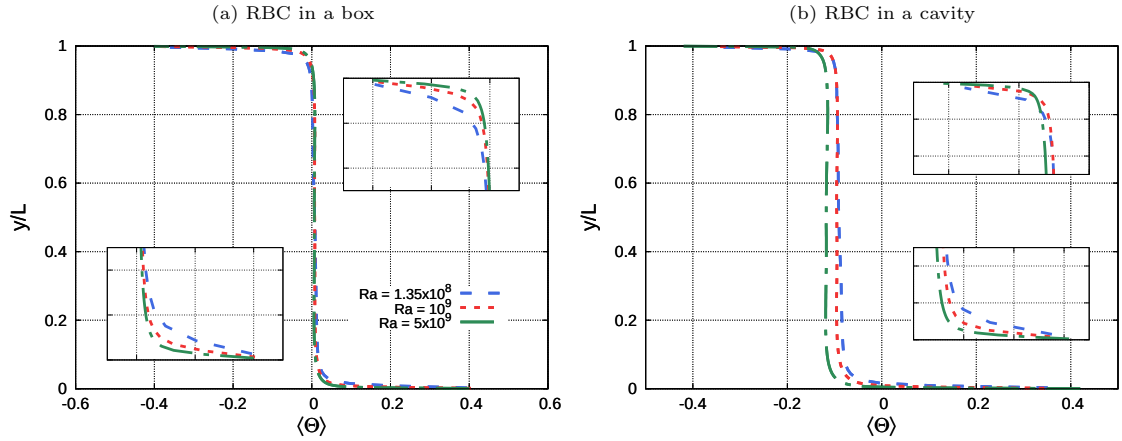


Fig. 13 WMLES with the KC1 model at different Ra: profiles of mean (time and area-averaged) normalized temperature $\langle \Theta \rangle$. The inserts show the zoom of these profiles near the top and bottom boundaries respectively. (a) RBC in box; (b) RBC in a cavity

The profiles of the (local) Nusselt number $Nu(y)$ are plotted in Figures 14a and 14b for RBC in a box and in a cavity, respectively. These profiles are not perfectly vertical as they should be, but exhibit a small tilt. As explained above, this is a numerical artifact attributed to the coarseness of the LES grid in the bulk. Also, in Table 10, we provide the WMLES predictions for the (global) Nusselt numbers and the estimates from correlations; RBC in a box in equation (28) and RBC in

a cavity in equation (29). Overall, the WMLES predictions for RBC in a box are very close to the estimates from correlation (28); the discrepancy between these values is approximately 1% even at high Rayleigh numbers. On the other hand, in the case of a cavity, the discrepancy between WMLES predictions and correlation (29) becomes larger as the Rayleigh number increases. More specifically, the discrepancy is 1.4% at $Ra = 1.35\times10^8$, 5.2% at $Ra = 10^9$ and 10.9% at $Ra = 5\times10^9$. As elaborated in the previous section, part of this divergence may be attributed to the fact that equation (29) was derived from numerical results at lower Ra and also accounts for evaporation across the free surface.

With regard to the numerical errors in the profiles of $Nu(y)$, it is worth recalling that the grid resolution in the bulk is based on estimates of the Nusselt number from $Nu - Ra$ correlations. As mentioned above, the correlation (29) that we used for RBC in a cavity was derived from simulations at lower Ra with evaporation across the free surface. It is therefore conceivable that more accurate correlations can be derived from experiments at high Ra. This, in turn, would lead to a more judicious selection of the grid resolution in the bulk for both WRLES and WMLES.

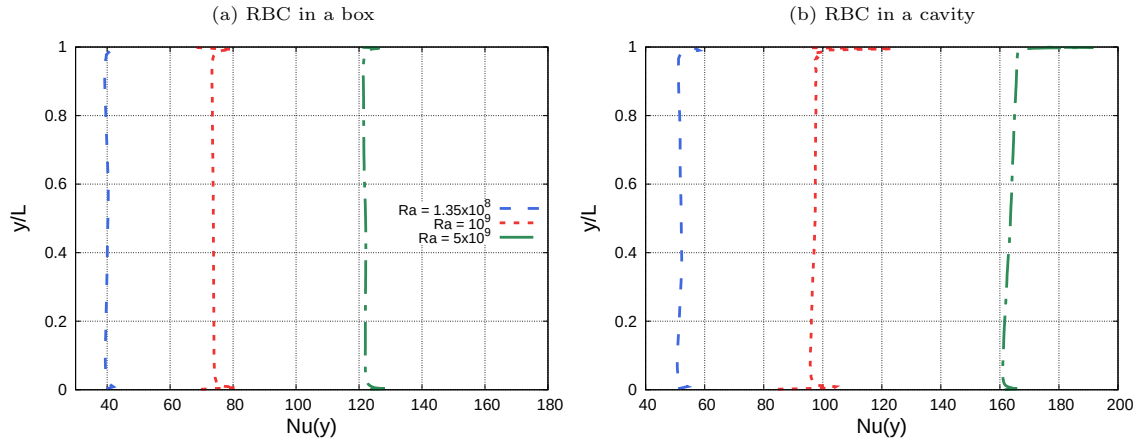


Fig. 14 WMLES with the KC1 model at different Ra: profiles of the (local) Nusselt number $Nu(y)$. (a) RBC in a box; (b) RBC in a cavity

Table 10 Nusselt number from WMLES at different Rayleigh numbers. The listed values are the averages of the computed profiles of $Nu(y)$; the second column shows the values based on the correlation (28) for RBC in a box and (29) for RBC in a cavity

	Box		Cavity	
Ra	Corr. (28)	WMLES KC1	Corr. (29)	WMLES KC1
1.35×10^8	40.3	39.7	49.8	50.5
10^9	74.9	73.7	91.1	95.8
5×10^9	123.1	121.8	147.8	163.9

In Figures 15a and 15b, we show the profiles of Θ_{rms} at different Ra for RBC in a box and in a cavity, respectively. These plots confirm that the fluctuations in the bulk decrease monotonically with the Rayleigh number for both configurations (box and cavity). Similarly, the peak values near the boundaries mildly decrease as Ra gets higher. While the locations of these peaks move closer

to the boundaries. In other words, the thickness of the thermal boundary layers decreases as the turbulence intensity increases, as expected.

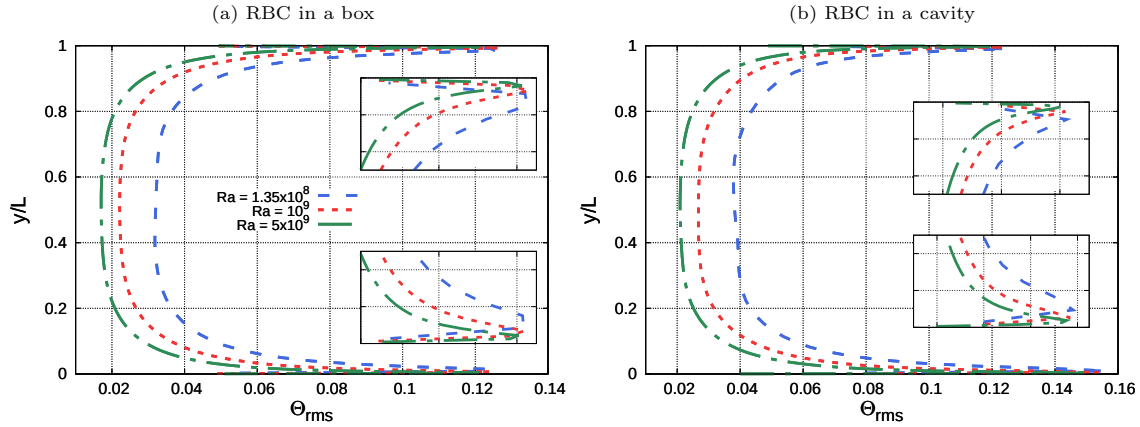


Fig. 15 WMLES with the KC1 model at different Ra: profiles of rms of the fluctuations of the normalized temperature, $\Theta_{\rm rms}$. The inserts show the zoom of these profiles near the top and bottom boundaries respectively. (a) RBC in a box; (b) RBC in a cavity

In Table 11, we compare the predictions of the WMLES for the thicknesses of the boundary layers with those from the estimates for the velocity in equation (30) and for the temperature in equation (31). Overall, the WMLES predictions are quite close to the estimated values, for both the hydrodynamic and thermal layers. The maximum discrepancy is approximately 7% for $\hat{\delta}_u$ and 9% for $\hat{\delta}_\theta$. It is also interesting to observe that in the case of RBC in a cavity, the WMLES prediction for the thickness of the top layer coincides with the estimate from equation (31). This is suggestive of the appropriateness of the KC1 model for free-slip layers even at high Ra.

Table 11 WMLES with the KC1 model at different $Ra = 5{\times}10^9$: comparison of the predictions for the thicknesses of the hydrodynamic and thermal boundary layers at the bottom and top boundaries; the notation is the same as in Table 6

	Bottom		Top
	$\hat{\delta}_u^{\rm wm}/\hat{\delta}_u^{\rm es}$	$\hat{\delta}_\theta^{\rm wm}/\hat{\delta}_\theta^{\rm es}$	$\hat{\delta}_\theta^{\rm wm}/\hat{\delta}_\theta^{\rm es}$
Box	1.07	1.05	1.05
Cavity	1.01	1.09	1.00

Finally, in Figures 16, we have plotted the profiles of the rms of the in-plane and vertical velocity fluctuations, $\overline{u}_{\rm rms}$ and $v_{\rm rms}$, respectively. According to them, the rms values in the bulk increase with Ra, as expected, and so do the peak values of $\overline{u}_{\rm rms}$ near the walls. Additionally, the locations of these peaks move closer to the walls as Ra increases, *i.e.* the thickness of the hydrodynamic boundary layer decreases with Ra. We may therefore conclude that the predictions for the case of high turbulence intensity, $Ra = 5{\times}10^9$, are consistent with those at lower intensities. We can also observe that, in the case of RBC in a cavity, the global peak of $\overline{u}_{\rm rms}$ occurs always at the top free-slip boundary and its value increases with Ra, as expected.

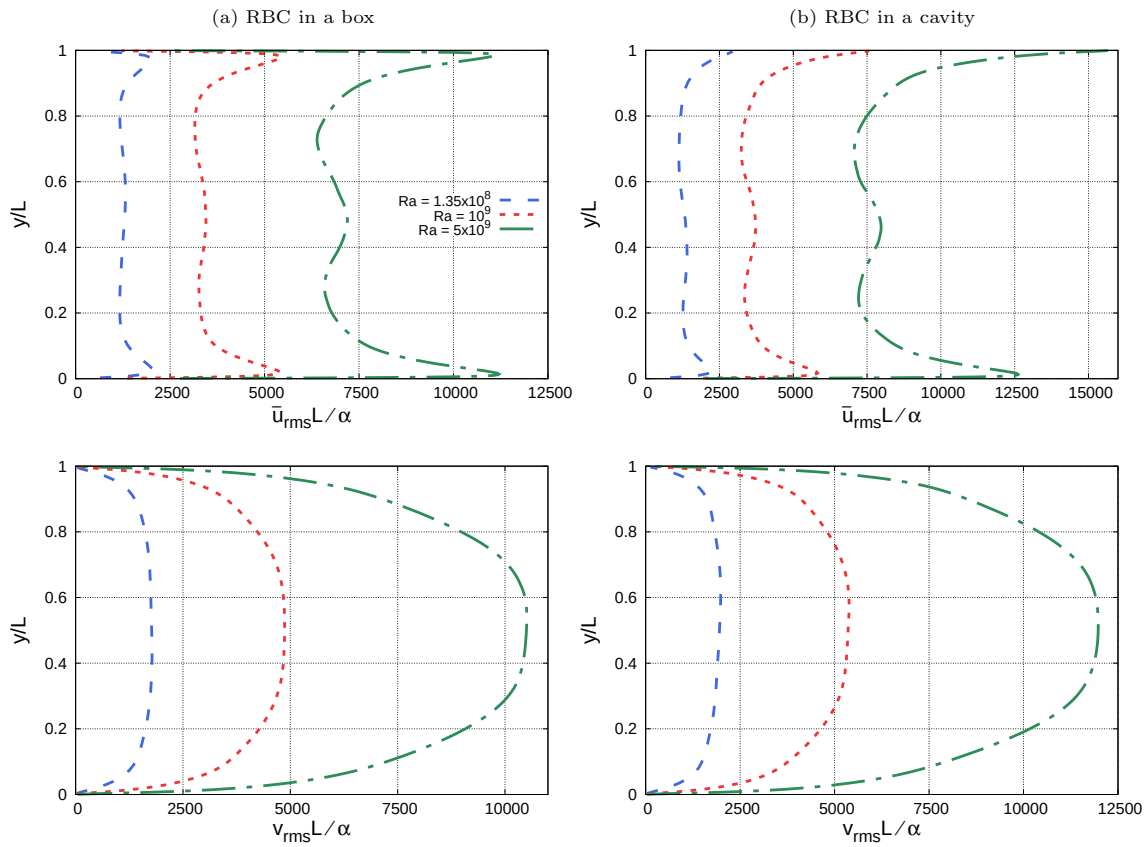


Fig. 16 WMLES with the KC1 model at different Ra: profiles of the rms of the normalized in-plane and vertical velocity fluctuations. (a) RBC in a box; (b) RBC in a cavity

Overall, the WMLES with the KC1 model predicts that natural convection at $Ra = 5{\times}10^9$ has the same features and properties as convection at $Ra = 1.35{\times}10^8$ and $Ra = 10^9$. Also, the KC1 model is robust enough to handle high turbulence intensities for convection both in a box and in a cavity.

6 Conclusion

In this paper, we have considered four different thermal boundary models for WMLES of natural convection of liquid water. We have considered two configurations: RBC in a box and RBC in a cavity with a free-slip top boundary. The predictive capacity of the thermal boundary models was assessed via comparisons through WRLES at two Rayleigh numbers; $Ra = 1.35{\times}10^8$ and $Ra = 10^9$.

Among these models, the Kays & Crawford ones (KC1 and KC2) performed well for both configurations. Their overall accuracy was comparable but the KC1 model has the advantage that is somewhat easier to implement. The Reynolds analogy (RA) model performed well in the case of RBC in a box. However, it gave mildly less accurate results for RBC in a cavity than KC1 and KC2 did. The main reason for this is that the model assumes a constant turbulent Prandtl number, which results in errors in the prediction of the turbulent conductivity in the vicinity of the top free-slip boundary. In absence of shear stresses, the turbulence viscosity is higher at the free-slip boundary, which impacts the prediction of the turbulent thermal conductivity and leads overestimating the heat exchange occurring at the surface. The Kader model is based on the temperature profile inside the boundary layer as an analogy to the law of the wall for the velocity. However, it cannot treat

free-slip boundaries because it becomes singular when the friction velocity vanishes. Further, for RBC in a box, it underperformed the other models and exhibited stability issues which could only be resolved by increasing the grid resolution near the walls.

Overall, on the basis of comparisons between WRLES and WMLES, our conclusion is that the KC1 had the most satisfactory performance in terms of grid size, computing time and accuracy.

Further, we performed WMLES of convection in a box and in a cavity with the KC1 model at a higher Rayleigh number, namely, $Ra = 5{\times}10^9$. The model was robust enough to handle this case and its numerical predictions are deemed quite reasonable.

As mentioned above, WMLES offers considerable computational savings and, therefore, has the potential to treat cases at higher turbulence intensities than those that DNS or WRLES can. However, this also implies that the performance of the various boundary models in those cases at higher Ra has to be tested via comparisons with experiments.

Acknowledgements. The authors gratefully acknowledge the financial support provided by the Belgian Federal Public Service Economy.

Declarations

- Funding: This research was funded by the Belgian Federal Public Service Economy under the Energy Transition Fund, project SFP-LOCA.
- Conflict of interest/Competing interests: The authors declare that they have no conflict of interest.
- Data availability: All data are available upon request.

References

Ahlers, G., Bodenschatz, E., Hartmann, R., He, X., Lohse, D., Reiter, P., Stevens, R.J., Verzicco, R., Wedi, M., Weiss, S., *et al.*: Aspect ratio dependence of heat transfer in a cylindrical Rayleigh-Bénard cell. Phys. Rev. Lett. **128**(8), 084501 (2022)

Ahlers, G., Grossmann, S., Lohse, D.: Heat transfer and large scale dynamics in turbulent Rayleigh-Bénard convection. Rev. Mod. Phys. **81**(2), 503–537 (2009)

Balay, S., Abhyankar, S.e.a.: PETSc users manual. Technical Report ANL-95/11 - Revision 3.11, Argonne National Laboratory (2019)

Benarafa, Y., Cioni, O., Ducros, F., Sagaut, P.: Temperature wall modelling for Large-Eddy-Simulation in a heated turbulent plane channel flow. Int. J. Heat Mass Tran. **50**(21-22), 4360–4370 (2007)

Bose, S.T., Park, G.I.: Wall-modeled large eddy simulation for complex turbulent flows. Annu. Rev. Fluid Mech. **50**(1), 535–561 (2018)

Bodenschatz, E., Pesch, W., Ahlers, G.: Recent developments in Rayleigh-Bénard convection. Annu. Rev. Fluid Mech. **32**(1), 709–778 (2000)

Baïri, A., Zarco-Pernia, E., De María, J.-M.G.: A review on natural convection in enclosures for engineering applications. The particular case of the parallelogrammic diode cavity. Appl. Therm.

Eng. **63**(1), 304–322 (2014)

Cabot, W., Moin, P.: Approximate wall boundary conditions in the Large-Eddy-Simulation of high Reynolds number flow. Flow Turbul. Combust. **63**, 269–291 (2000)

Choi, H., Moin, P.: Grid-point requirements for Large-Eddy-Simulation: Chapman's estimates revisited. Phys. Fluids **24**(1), 011702 (2012)

Chillà, F., Schumacher, J.: New perspectives in turbulent Rayleigh-Bénard convection. Eur. Phys. J. E **35**(7), 58 (2012)

Eidson, T.M.: Numerical simulation of the turbulent Rayleigh-Bénard problem using subgrid modelling. J. Fluid Mech. **158**, 245–268 (1985)

Foroozani, N., Niemela, J., Armenio, V., Sreenivasan, K.: Reorientations of the large-scale flow in turbulent convection in a cube. Phys. Rev. E **95**, 033107 (2017)

Ferziger, J.H., Perić, B., Street, R.L.: Computational Methods for Fluid Dynamics, 4th edn. Springer, New York (2019)

Grossmann, S., Lohse, D.: Scaling in thermal convection: a unifying theory. J. Fluid Mech. **407**, 27–56 (2000)

Grossmann, S., Lohse, D.: Thermal convection for large Prandtl numbers. Phys. Rev. Lett. **86**(15), 3316–3319 (2001)

Grossmann, S., Lohse, D.: Multiple scaling in the ultimate regime of thermal convection. Phys. Fluids **23**(4) (2011)

Hartmann, D.L., Moy, L.A., Fu, Q.: Tropical convection and the energy balance at the top of the atmosphere. J. Climate **14**(24), 4495–4511 (2001)

Hay, W.A., Martin, J., Migot, B., Papalexandris, M.V.: Turbulent thermal convection driven by free-surface evaporation in cuboidal domains of different aspect ratios. Phys. Fluids **33**(1), 015104 (2021)

Hay, W.A., Papalexandris, M.V.: Numerical simulations of turbulent thermal convection with a free-slip upper boundary. P. Roy. Soc. A-Math. Phy. **475**(2232), 20190601 (2019)

Hay, W.A., Papalexandris, M.V.: Evaporation-driven turbulent convection in water pools. J. Fluid Mech. **904**, 14 (2020)

Kader, B.: Temperature and concentration profiles in fully turbulent boundary layers. Int. J. Heat Mass Tran. **24**(9), 1541–1544 (1981)

Kays, W.M.: Turbulent Prandtl number. Where are we? ASME J. Heat Trans. **116**(2), 284–295 (1994)

Kays, W.M., Crawford, M.E.: Convective Heat and Mass Transfer, 3rd edn. McGraw-Hill, New York

(1993)

Kenjereš, S., Hanjalić, K.: LES, T-RANS and hybrid simulations of thermal convection at high *Ra* numbers. Int. J. Heat Fluid Fl. **27**(5), 800–810 (2006)

Kawai, S., Larsson, J.: Wall-modeling in Large-Eddy-Simulation: Length scales, grid resolution, and accuracy. Phys. Fluids **24**(1) (2012)

Kahraman, A.B., Larsson, J.: Adaptive determination of the optimal exchange location in wall-modeled Large-Eddy-Simulation. AIAA J. **60**(7), 4162–4173 (2022)

Lemmon, E.W., Huber, M.L., McLinden, M.O.: NIST Standard Reference Database 23: Reference Fluid Thermodynamic and Transport Properties - REFPROP, 9.0 edn. Gaithersburg (2010)

Larsson, J., Kawai, S., Bodart, J., Bermejo-Moreno, I.: Large-Eddy-Simulation with modeled wall-stress: recent progress and future directions. Mech. Eng. Rev. **3**(1), 15–00418 (2016)

Lessani, B., Papalexandris, M.V.: Time-accurate calculation of variable density flows with strong temperature gradients and combustion. J. Comput. Phys. **212**(1), 218–246 (2006)

Lessani, B., Papalexandris, M.V.: Numerical study of turbulent channel flow with strong temperature gradients. Int. J. Numer. Method. H **18**, 545–556 (2008)

Lohse, D., Xia, K.-Q.: Small-scale properties of turbulent rayleigh-bénard convection. Ann. Rev. Fluid Mech. **42**, 335–364 (2010)

Lau, G., Yeoh, G., Timchenko, V., Reizes, J.: Large-Eddy-Simulation of natural convection in an asymmetrically-heated vertical parallel-plate channel: Assessment of subgrid-scale models. Comput. Fluids **59**, 101–116 (2012)

Meneveau, C., Lund, T.S., Cabot, W.H.: A Lagrangian dynamic subgrid-scale model of turbulence. J. Fluid Mech. **319**, 353–385 (1996)

Marichal, J., Papalexandris, M.V.: On the dynamics of the large scale circulation in turbulent convection with a free-slip upper boundary. Int. J. Heat Mass Tran. **183**, 122220 (2022)

Marshall, J., Schott, F.: Open-ocean convection: Observations, theory, and models. Rev. Geophys. **37**(1), 1–64 (1999)

Nicoud, F., Ducros, F.: Subgrid-scale stress modelling based on the square of the velocity gradient tensor. Flow Turbul. Combust. **62**, 183–200 (1999)

Niemela, J.J., Skrbek, L., Sreenivasan, K.R., Donnelly, R.J.: Turbulent convection at very high Rayleigh numbers. Nature **404**(6780), 837–840 (2000)

Paolucci, S.: Filtering of sound from the Navier–Stokes equations. NASA STI/Recon Technical Report N **83**, 26036 (1982)

Papalexandris, M.V.: On the applicability of Stokes' hypothesis to low-Mach-number flows.

Continuum Mech. Therm. **32**(4), 1245–1249 (2020)

Piomelli, U., Balaras, E.: Wall-layer models for Large-Eddy-Simulations. Annu. Rev. Fluid Mech. **34**, 349–74 (2002)

Peng, S.-H., Davidson, L.: Large-Eddy-Simulation for turbulent buoyant flow in a confined cavity. Int. J. Heat Fluid Fl. **22**, 323–331 (2001)

Peng, S.-H., Davidson, L.: On a subgrid-scale heat flux model for Large-Eddy-Simulation of turbulent thermal flow. Int. J. Heat Mass Tran. **45**(7), 1393–1405 (2002)

Peng, S.-H., Hanjalic, K., Davidson, L.: Large-Eddy-Simulation and deduced scaling analysis of Rayleigh-Bénard convection up to $Ra = 10^9$. J. Turbul. **7**, 66 (2006)

Pope, S.B.: Turbulent Flows. Cambridge University Press, Cambridge (2003)

Ramponi, R., Blocken, B.: CFD simulation of cross-ventilation for a generic isolated building: Impact of computational parameters. Build. Environ. **53**, 34–48 (2012)

Reichardt, H.: The principles of turbulent heat transfer, Transl. by PA Scheck in Recent Advances in Heat and Mass Transfer, ed. by JP Hartnett. McGraw-Hill, Boston (1961)

Sagaut, P.: Large Eddy Simulation for Incompressible Flows, 3rd edn. Springer, Berlin (2006)

Sarić, S., Basara, B., Zunic, Z.: Advanced near-wall modeling for engine heat transfer. Int. J. Heat Fluid Fl. **63**, 205–211 (2017)

Sugiyama, K., Calzavarini, E., Grossmann, S., Lohse, D.: Flow organization in two-dimensional non-Oberbeck–Boussinesq Rayleigh–Bénard convection in water. J. Fluid Mech. **637**, 105–135 (2009)

Sarbu, I., Dorca, A.: Review on heat transfer analysis in thermal energy storage using latent heat storage systems and phase change materials. Int. J. Energ. Res. **43**(1), 29–64 (2019)

Silva, M.C., De Lima, L.C., Miranda, R.F.: Comparative analysis of different models for the turbulent Prandtl number. J. Heat Transf. **121**(2), 473–477 (1999)

Shishkina, O.: Rayleigh-Bénard convection: The container shape matters. Phys. Rev. Fluids **6**(9), 090502 (2021)

Shishkina, O., Stevens, R.J., Grossmann, S., Lohse, D.: Boundary layer structure in turbulent thermal convection and its consequences for the required numerical resolution. New J. Phys. **12**(7), 075022 (2010)

Shishkina, O., Thess, A.: Mean temperature profiles in turbulent Rayleigh–Bénard convection of water. J. Fluid Mech. **633**, 449–460 (2009)

Stevens, R.J.A.M., Verzicco, R., Lohse, D.: Radial boundary layer structure and Nusselt number in Rayleigh–Bénard convection. J. Fluid Mech. **643**, 495–507 (2010)

Valencia, L., Pallares, J., Cuesta, I., Grau, F.X.: Rayleigh-Bénard convection of water in a perfectly conducting cubical cavity: effects of temperature-dependent physical properties in laminar and turbulent regimes. Numer. Heat Tr. A-Appl. **47**(4), 333–352 (2005)

Valencia, L., Pallares, J., Cuesta, I., Grau, F.X.: Turbulent Rayleigh–Bénard convection of water in cubical cavities: A numerical and experimental study. Int. J. Heat Mass Tran. **50**(15-16), 3203–3215 (2007)

Weigand, B., Ferguson, J., Crawford, M.: An extended Kays and Crawford turbulent Prandtl number model. Int. J. Heat Mass Tran. **40**(17), 4191–4196 (1997)

Wong, V., Lilly, D.K.: A comparison of two dynamic subgrid closure methods for turbulent thermal convection. Phys. Fluids **6**(2), 1016–1023 (1994)

Wang, Q., Liu, H.-R., Verzicco, R., Shishkina, O., Lohse, D.: Regime transitions in thermally driven high-Rayleigh number vertical convection. J. Fluid Mech. **917**, 6 (2021)

Yilmaz, I.: Parallel direct numerical simulation and analysis of turbulent Rayleigh-Bénard convection at moderate Rayleigh numbers using an efficient algorithm. Comput. Fluids **213**, 104754 (2020)

Zikanov, O., Slinn, D.N., Dhanak, M.R.: Turbulent convection driven by surface cooling in shallow water. J. Fluid Mech. **464**, 81–111 (2002)